ENC 2012
EUROPEAN NUCLEAR CONFERENCE

Transactions Nuclear Data

EUROPEAN NUCLEAR SOCIETY

ENS CONFERENCE

ENC 2012 Diamond Sponsor:

HITACHI

ENC 2012 Gold Sponsors:

AGORIA
no future without technology

Belgoprocess

SCK·CEN
STUDIECENTRUM VOOR KERNENERGIE
CENTRE D'ETUDE DE L'ENERGIE NUCLEAIRE

NUCLEAIR FORUM NUCLEAIRE

ENC 2012 Silver Sponsor:

urenco

ENC 2012 Sponsor:

ONET TECHNOLOGIES

organised in collaboration with:

the Nuclear Institute

IAEA International Atomic Energy Agency

NEA Nuclear Energy Agency

European Nuclear Society
Rue Belliard 65
1040 Brussels, Belgium
Phone + 32 2 505 30 54
Fax +32 2 502 39 02
E-mail ens@euronuclear.org
Internet www.euronuclear.org

ISBN 978-92-95064-14-0

These transactions contain all contributions submitted by 7 December 2012.

ENC2012-A0021	High-precision measurement of the 238U(n,γ) cross section at nTOF, CERN	Wright, T. (1); Billowes, J. (1); Ware, T. (1); Guerrero, C. (2); Cano ott, D. (3); Gunsing, F. (4); Berthoumieux, E. (4); Lampoudis, C. (5); Massimi, C. (6); Mingrone, F. (6); The n_tof collaboration, (2) 1 - University of Manchester, United Kingdom 2 - CERN, Switzerland 3 - CIEMAT, Spain 4 - CEA, France 5 - EC-JRC-IRMM, Belgium 6 - INFN, Italy
ENC2012-A0100	SPECTRAL CORRECTION FOR NUCLEAR DATA IN FAST REACTOR ANALYSIS VIA THE SUBGROUP DECOMPOSITION METHOD	Douglass, S. (1); Rahnema, F. (1) 1 - Georgia Institute of Technology, United States
ENC2012-A0129	Measurement of the 243Am neutron capture cross section at the n_TOF facility at CERN	Mendoza Cembranos, E. (1); Cano Ott, D. (1); Guerrero Sánchez, C. (2); , T. N. C. (2) 1 - CIEMAT, Spain 2 - CERN, Switzerland
ENC2012-A0246	ELECTRA Core Dynamics and Stability Analyses	Bortot, S. (1); Suvdantsetseg, E. (1); Wallenius, J. (1); Lorenzi, S. (2); Della Bona, A. (2) 1 - KTH, Sweden 2 - Politecnico di Milano, Italy
ENC2012-A0274	ANALYSIS OF THE TUBES-TO-TUBESHEET CREVICES UNDER THE OPERATING CONDITIONS OF THE AP1000 PRHR-HX	Barbensi, A. (1) 1 - Ansaldo Nucleare S.p.A., Italy

NUCLEAR DATA

HIGH-PRECISION MEASUREMENT OF THE ^{238}U(n,γ) CROSS SECTION AT n_TOF/CERN

T. Wright[1], C. Guerrero[2], J. Billowes[1], T. Ware[1], D. Cano-Ott[3], E. Mendoza[3], S. Altstadt[4], J. Andrzejewski[5], L. Audouin[6], M. Barbagallo[7], V. Bécares[3], F. Bečvář[8], F. Belloni[9], E. Berthoumieux[9,2], V. Boccone[2], D. Bosnar[10], M. Brugger[2], M. Calviani[2], F. Calviño[11], C. Carrapiço[12], F. Cerutti[2], E. Chiaveri[9,2], M. Chin[2], N. Colonna[7], G. Cortés[11], M.A. Cortés-Giraldo[13], M. Diakaki[14], C. Domingo-Pardo[15], I. Duran[16], N. Dzysiuk[17], C. Eleftheriadis[18], A. Ferrari[2], K. Fraval[9], S. Ganesan[19], A.R. Garcìa[3], G. Giubrone[15], M.B. Gómez-Hornillos[11], I.F. Gonçalves[12], E. González-Romero[3], E. Griesmayer[20], F. Gunsing[9], P. Gurusamy[19], D.G. Jenkins[21], E. Jericha[20], Y. Kadi[2], F. Käppeler[22], D. Karadimos[14], P. Koehler[23], M. Kokkoris[14], M. Krtička[8], J. Kroll[8], C. Langer[4], C. Lederer[4,24], H. Leeb[20], L.S. Leong[6], R. Losito[2], A. Manousos[18], J. Marganiec[5], T. Martìnez[3], C. Massimi[25], P.F. Mastinu[17], M. Mastromarco[7], M. Meaze[7], A. Mengoni[26], P.M. Milazzo[27], F. Mingrone[25], M. Mirea[28], W. Mondalaers[29], C. Paradela[16], A. Pavlik[24], J. Perkowski[5], A. Plompen[29], J. Praena[13], J.M. Quesada[13], T. Rauscher[30], R. Reifarth[4], A. Riego[11], F. Roman[2,28], C. Rubbia[2,31], R. Sarmento[12], P. Schillebeeckx[29], S. Schmidt[4], G. Tagliente[7], J.L. Tain[15], D. Tarrìo[16], L. Tassan-Got[6], A. Tsinganis[2], S. Valenta[8], G. Vannini[25], V. Variale[7], P. Vaz[12], A. Ventura[26], R. Versaci[2], M.J. Vermeulen[21], V. Vlachoudis[2], R. Vlastou[14], A. Wallner[24], M. Weigand[4], C. Weiß[20], P. Žugec[10], The n_TOF Collaboration (www.cern.ch/ntof)

1) University of Manchester, Oxford Road, Manchester, UK
2) European Organization for Nuclear Research (CERN), Geneva, Switzerland
3) Centro de Investigaciones Energeticas Medioambientales y Tecnológicas (CIEMAT), Madrid, Spain
4) Johann-Wolfgang-Goethe Universität, Frankfurt, Germany
5) Uniwersytet Łódzki, Lodz, Poland
6) Centre National de la Recherche Scientifique/IN2P3 - IPN, Orsay, France
7) Istituto Nazionale di Fisica Nucleare, Bari, Italy
8) Charles University, Prague, Czech Republic
9) Commissariat à l'Énergie Atomique (CEA) Saclay - Irfu, Gif-sur-Yvette, France
10) Department of Physics, Faculty of Science, University of Zagreb, Croatia
11) Universitat Politecnica de Catalunya, Barcelona, Spain
12) Instituto Tecnológico e Nuclear, Instituto Superior Técnico, Universidade Técnica de Lisboa, Lisboa, Portugal
13) Universidad de Sevilla, Spain
14) National Technical University of Athens (NTUA), Greece
15) Instituto de Fìsica Corpuscular, CSIC-Universidad de Valencia, Spain
16) Universidade de Santiago de Compostela, Spain
17) Istituto Nazionale di Fisica Nucleare, Laboratori Nazionali di Legnaro, Italy
18) Aristotle University of Thessaloniki, Thessaloniki, Greece
19) Bhabha Atomic Research Centre (BARC), Mumbai, India
20) Atominstitut, Technische Universität Wien, Austria
21) University of York, Heslington, York, UK
22) Karlsruhe Institute of Technology, Campus Nord, Institut für Kernphysik, Karlsruhe, Germany
23) Oak Ridge National Laboratory (ORNL), Oak Ridge, TN 37831, USA
24) University of Vienna, Faculty of Physics, Austria
25) Dipartimento di Fisica, Università di Bologna, and Sezione INFN di Bologna, Italy
26) Agenzia nazionale per le nuove tecnologie, l'energia e lo sviluppo economico sostenibile (ENEA), Bologna, Italy
27) Istituto Nazionale di Fisica Nucleare, Trieste, Italy
28) Horia Hulubei National Institute of Physics and Nuclear Engineering - IFIN HH, Bucharest - Magurele, Romania
29) European Commission JRC, Institute for Reference Materials and Measurements, Retieseweg 111, B-2440 Geel, Belgium
30) Department of Physics and Astronomy - University of Basel, Basel, Switzerland
31) Laboratori Nazionali del Gran Sasso dell'INFN, Assergi (AQ),Italy

ABSTRACT

The neutron capture cross section of ^{238}U is fundamental to future fast nuclear reactors, and thus must be measured to an extremely high level of accuracy. A measurement was performed at the CERN n_TOF facility with two sets of detectors: two C_6D_6 liquid scintillators and a 4π Total Absorption Calorimeter (TAC) consisting of 40 BaF_2 crystals. A preliminary analysis of the TAC data is presented where one can see the high accuracy of the measurement in the resolved resonance region between 1 eV and 20 keV.

1. **Introduction**

The present accuracy of the neutron capture cross section of ^{238}U is high compared to other isotopes but still imposes some limitations to the simulation of operating nuclear reactors and "Generation-III+" Light Water Reactors, as well as "Generation-IV" reactor designs. Indeed, sizable inconsistencies appear when comparing previous measurements in the epithermal energy region up to 25 keV. As such, measurements to reduce these uncertainties on the ^{238}U capture cross section have been placed on the NEA High Priority Request List (1). In this context, the *Accurate Nuclear Data for nuclear Energy Sustainability* (ANDES) (2) project of the European Commission 7th Framework Programme aims to achieve the required precision and improve the existing measurements of the ^{238}U cross section. This neutron capture cross section has thus been measured at the n_TOF facility (3) at CERN with two different detector set-ups, and also at GELINA (4) at EC-JRC-IRMM. These three measurements are now being analyzed in common with the aim of reducing the uncertainty in the cross section down to 2%, leading to the most accurate ^{238}U neutron capture cross section to date.

2. **The cross section measurement at CERN**

The measurement of the ^{238}U capture cross section was carried out with the 4π Total Absorption Calorimeter (TAC) (5) at the CERN neutron-spallation source n_TOF during 2011. The neutron time-of-flight n_TOF facility provides a pulsed neutron source produced from spallation reactions as 20 GeV/c protons from the CERN accelerator complex impinge on a lead target. This produces a white (10 meV to 20 GeV) neutron beam which is collimated along a 185 m beam line, leading to a high neutron energy resolution at the measurement station.

The TAC is an array of 40 BaF_2 scintillators covering 95% of the total solid angle. It features a high γ-ray total absorption efficiency, reasonable γ-ray energy resolution, high segmentation and fast time response. All these qualities make the TAC an ideal device for measuring capture cross sections with high accuracy, in this case ^{238}U cross section for the resolved energy range is measured up to 20 keV.

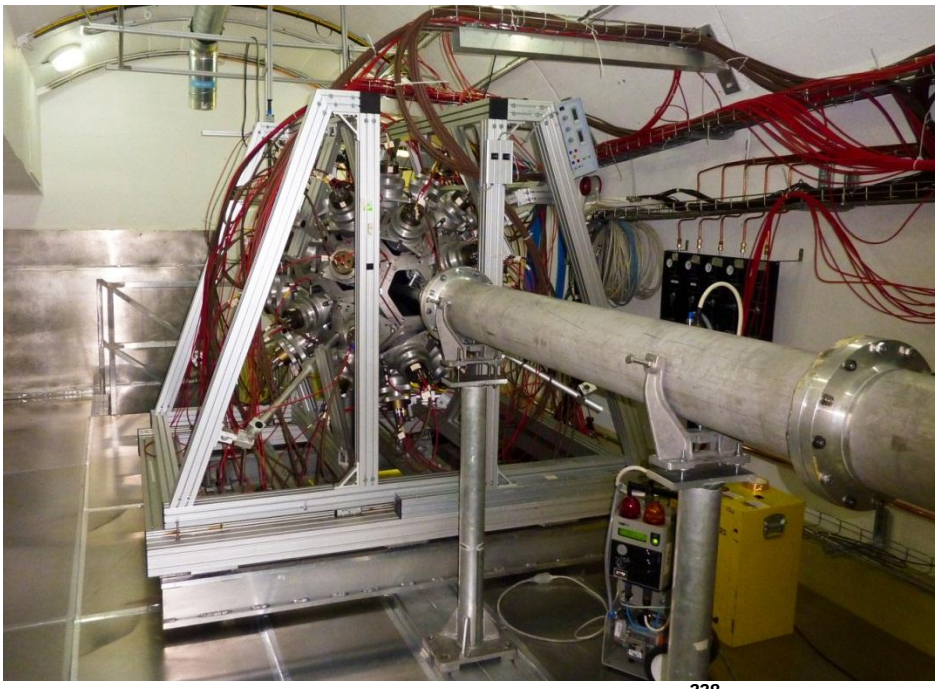

Figure 2.1. Photograph of the TAC setup during the $^{238}U(n,\gamma)$ experiment.

The high purity (>99.99%) metallic ^{238}U sample, produced and characterized by EC-JRC-IRMM, weighed 6.002 g, measured 53x30 mm^2 and was encased in 60 µm of Kapton and 75 µm of aluminum. The large sample nearly covered the full beam size, which ranges up to 4 cm in diameter. The sample was surrounded by a borated polyethylene neutron absorber to help reduce the TAC detection efficiency to neutrons scattered in the sample. The experiment also comprised of the measurement of a gold sample for normalization purposes, a carbon sample to determine the neutron scattering background and an empty sample frame to estimate the sample independent background.

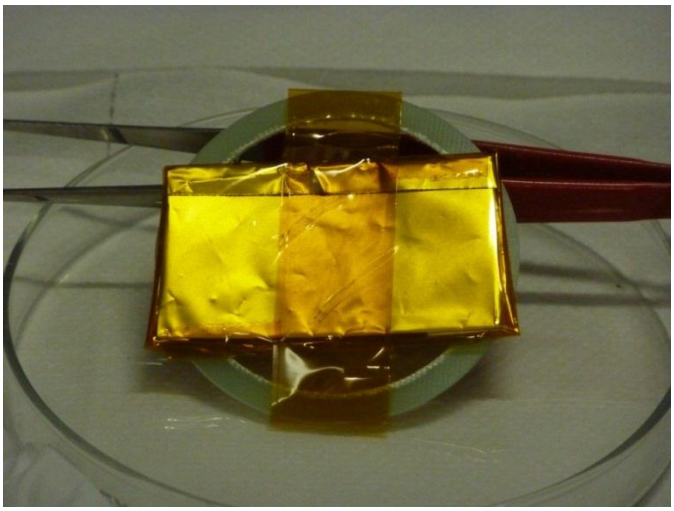

Figure 2.2. The ^{238}U sample encased in 60 µm Kapton and 75 µm aluminum.

Considering the large size and high mass of the ^{238}U sample, the intensity of the neutron beam was reduced a factor of 10 from its nominal value, since otherwise the reaction rate was too high and induced a sizable fraction of pile-up events in the TAC.

3. **Preliminary results**

The signals from the BaF_2 crystals are digitized at 250 MSample/s and stored for offline analysis. The basic information from each recorded pulse is extracted using a sophisticated pulse shape analysis routine (6) and the signals from the individual crystals are grouped together into events using a coincidence window of 20 ns. Each of these events is characterized by total the energy deposited in the TAC, the number of crystals (multiplicity) involved in the detection, and the time-of-flight t_{ToF}. The corresponding neutron energy E_n of the events is determined as

$$E_n(eV) = \left(\frac{(72.298.L(m)}{t_{ToF}(\mu s) - t_0(\mu s)}\right)^2,$$

where t_0 is the neutron production time and L is the length of the flight path.

The energy calibration of the individual crystals was performed periodically during the measurement using three standard calibration sources: ^{137}Cs (662 keV), ^{88}Y (898 and 1836 keV) and Am/Be (4440 keV). A second order polynomial was fitted to the four energy calibration points.

A benefit of the TAC with respect to other detection systems is that by selecting favorable analysis conditions in the energy deposited and the crystal multiplicity, one can vastly reduce the background contribution. The selected conditions which achieved a balance between background reduction and loss of efficiency were; crystal multiplicity greater than two, and deposited energy between 2.5 and 5.5 MeV. The reason for the latter is that the neutron separation energy of ^{238}U is 4.9 MeV, therefore any counts above this energy are not from neutron capture in ^{238}U but in other materials present in the set-up. The lower limit eliminates a large fraction of the low energy background; especially the 2.2 MeV γ- rays produced by neutron capture in the hydrogen of the neutron absorber following neutron scattering in the ^{238}U sample. The response of the TAC to the ^{238}U and background measurements is shown in Figure 3.1, where the analysis condition in deposited energy are indicated as vertical dashed lines. The peak from capture reactions in ^{238}U is observed at 4.9 MeV.

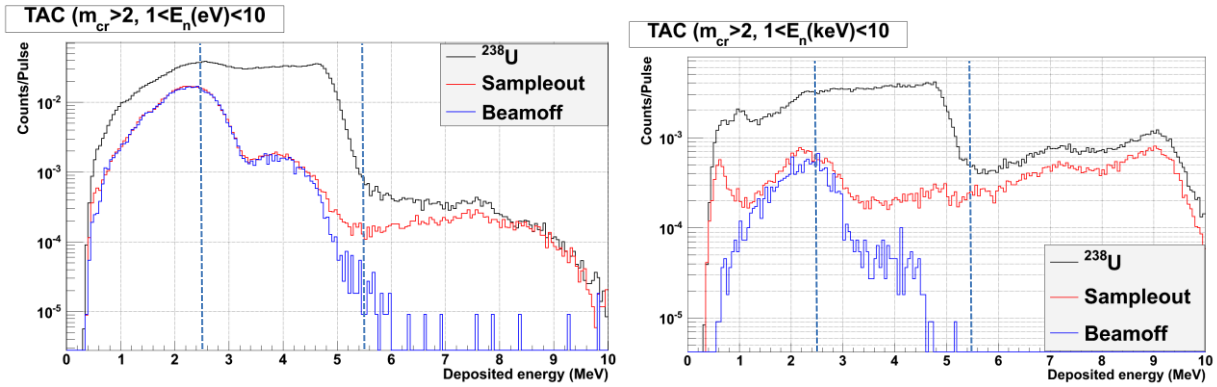

Figure 3.1. Deposited energy in the TAC for low (left) and high (right) neutron energy regions. The chosen analysis conditions are indicated as dashed vertical lines.

With the mentioned analysis conditions applied to the data, the distribution of detected events as a function of neutron energy were extracted. This is displayed in Figure 3.2 for the ^{238}U and background measurements. It is observed that the resonances from the capture cross section of

^{238}U are clearly visible above the background. The background is lower than 5% of the total counts even around 10 keV, where the resonances are not as intense as in the eV region.

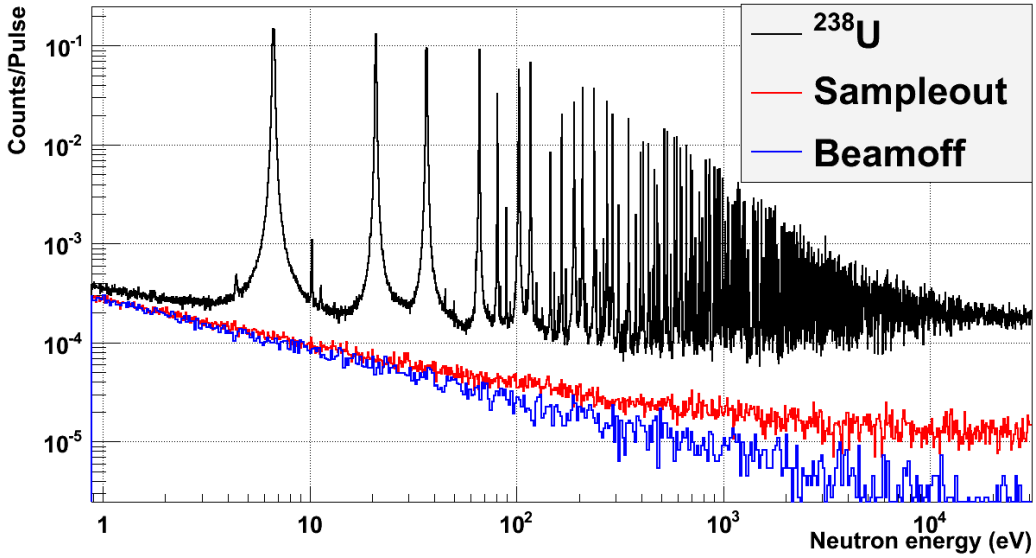

Figure 3.2. Neutron energy distribution of ^{238}U and background measurements. The analysis conditions of multiplicity > 2 and deposited energy between 2.5 and 5.5 MeV have been applied.

The high resolution and statistics of the measurements allow one to see well-resolved resonances at high energies. An example is given in Figure 3.3, which shows the neutron energy distribution of ^{238}U, after background subtraction, in the keV region.

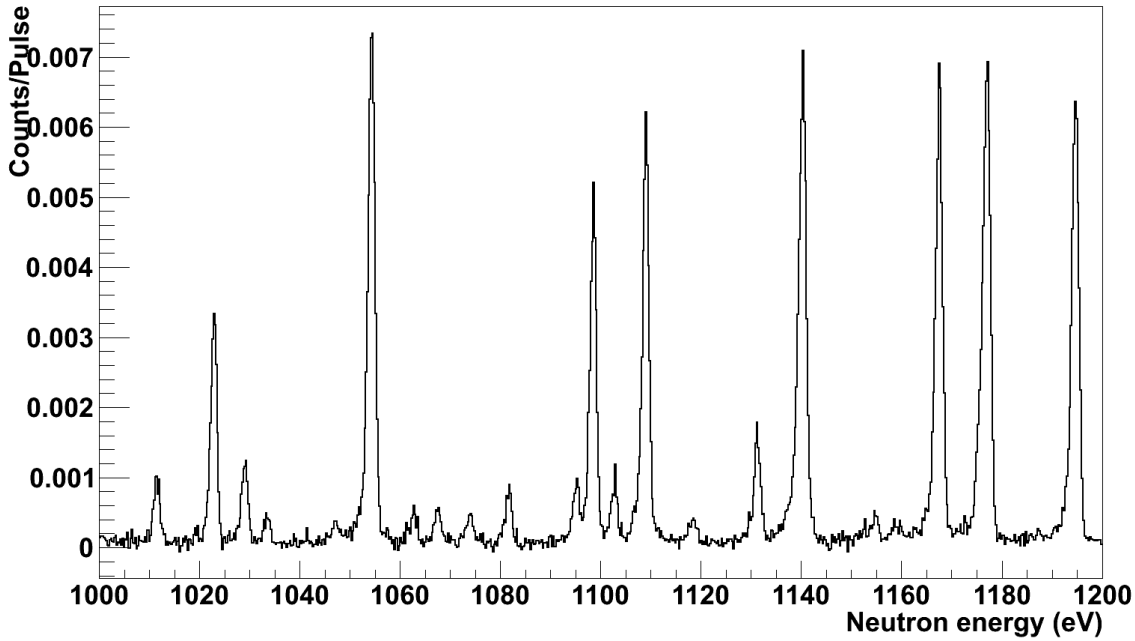

Figure 3.3. The ^{238}U counts with the sample out and beam off background subtracted

4. **Expected results**

The high energy resolution and statistics of the measurement have been demonstrated in the previous section. These allow one to obtain a capture yield of ^{238}U where the resonances are very well resolved up to high energies. However, reaching the high accuracy required for this measurement requires more than this, and it is necessary to minimize all the systematic uncertainties which propagate to the final cross section.

□

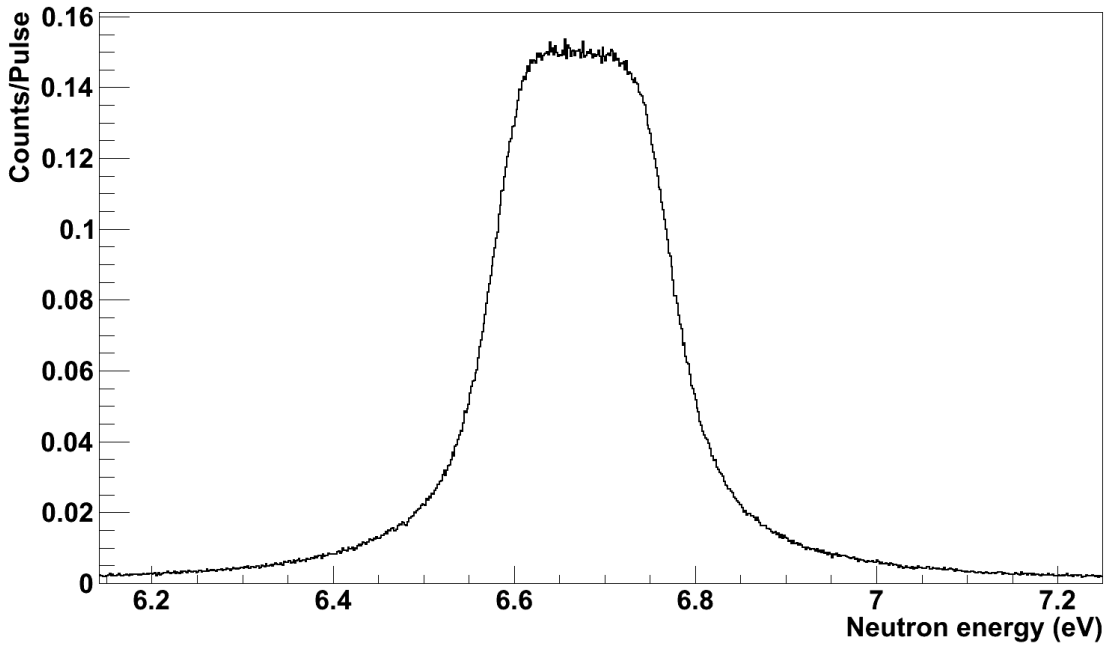

Figure 3.4. The first ^{238}U resonance features a flat top (saturation) resulting from all neutrons in the beam interacting with the ^{238}U sample.

The main sources of systematic uncertainty are the background subtraction, the pile-up correction and the determination of the incident neutron flux. The first has been shown to be minimized by the selection of the appropriate analysis conditions, and the second by the reduction of the neutron beam intensity. Regarding the third, the present experimental setup allows for maximal accuracy in determination of the neutron flux. Due to the thickness of the sample, the first three resonances are saturated (see Figure 3.4) (7), meaning that all the neutrons at the resonances energies interact with the sample and thus one can calculate very accurately the neutron flux at three different neutron energy values. This provides the absolute value of the neutron flux, while its neutron energy dependence has been calculated previously by measuring the standard ^{6}Li(n,α) and ^{10}B(n,α) cross sections.

The capture yield will be obtained in the neutron energy range from 0.3 eV to 20 keV and then analyzed with the R-matrix resonance analysis code SAMMY (8). The results will be cross checked with other codes such as REFIT (9). Following a preliminary analysis of the TAC data presented in this paper, these will be combined with the aforementioned C_6D_6 detector data from n_TOF and GELINA. The three data sets will be then used as input for a new evaluation of the ^{238}U capture cross section in the resolved resonance region.

5. **Conclusions**

The capture cross section of ^{238}U, of importance for the design of future nuclear energy systems, has been measured at the CERN n_TOF facility using the 4π BaF_2 Total Absorption Calorimeter. The measured data, covering the full resolved resonance region range (1 eV to 20 keV),

combine high neutron energy resolution and low background with high statistics and the existence of three saturated resonances. Such a combination allows one to extract a very accurate capture yield that will soon be analyzed in terms of resonance shape analysis with the SAMMY code. Finally, the results shall be combined with the C_6D_6 measurements carried out at CERN and GELINA to produce a new evaluated capture cross section. The results will be of the highest quality and shall represent an important contribution to the future nuclear data libraries.

6. Acknowledgements

The authors acknowledge financial support from the UK National Nuclear Laboratory (NNL), CERN, the EC-FP7 ANDES (FP7-249671) project, ENRESA under the CIEMAT-ENRESA agreement and the Spanish Ministry of Science and Innovation (FPA2005-06918-C03-01). This work is the core of the PhD thesis of Tobias Wright, who is sponsored by the UK Nuclear Decommissioning Authority (NDA).

7. References

1. NEA High Priority Request List. *http://www.oecd-nea.org/dbdata/hprl/.* [Online]
2. ANDES, Project FP7-249671 of the EURATOM FP7 . *http://www.andes-nd.eu/.* [Online]
3. *Performance of the neutron time-of-flight facility n_TOF at CERN.* **al., C. Guerrero et.** s.l. : submitted to Eur. Phys. J A (2012).
4. *Modeling of the GELINA neutron target using coupled electron–photon–neutron transport with the MCNP4C3 code.* **al., M. Flaska et.** 2004, Nuclear Instruments and Methods in Physics Research Section A, Vol. 531, pp. 392-406.
5. *The n_TOF Total Absorption Calorimeter for neutron capture measurements at CERN.* **al., C. Guerrero et.** s.l. : Nuclear Instruments and Methods in Physics Research A, Vol. 608 (2009).
6. **Berthoumieux, E.** *Preliminary report on BaF2 Total Absorption Calorimeter.* CEA-Saclay/DAPNIA/SPhN : s.n., 2004.
7. *Absolute neutron capture yield calibration.* **R.Macklin, J.Halperin, R.Winters.** s.l. : Nuclear Instruments and Methods, 1979, Vol. 164, pp. 213-214.
8. **Larson, N. M.** *Updated Users' Guide for SAMMY: Multilevel R-matrix Fits to Neutron Data Using Bayes' Equations.* Oak Ridge, TN, USA : ORNL/TM-9179/7, 2006.
9. **M. C. Moxon, T. C. Ware, C. J. Dean.** *REFIT-2009: A Least-Square Fitting Program for Resonance Analysis of Neutron Transmission, Capture, Fission and Scattering Data, Users' Guide for REFIT-2009-10.* s.l. : UKNSF(2010)P243.

SPECTRAL CORRECTION FOR NUCLEAR DATA IN FAST REACTOR ANALYSIS VIA THE SUBGROUP DECOMPOSITION METHOD

S. DOUGLASS, F. RAHNEMA
Nuclear and Radiological Engineering and Medical Physics Programs
George W. Woodruff School, Georgia Institute of Technology
770 State St., Atlanta, GA, 30332 – United States of America

ABSTRACT

Among the challenges of optically thin reactors is the reduced effectiveness of standard nuclear data condensation and homogenization methods, which rely on fine-group lattice-cell calculations with specular reflective boundary conditions to generate condensed multigroup nuclear data (cross sections). In fast reactors, the accuracy of these cross sections is reduced by the presence of a large number of lattice cells which do not possess fissionable material (e.g., control or reflector blocks) and are therefore unsuitable for the standard lattice (nuclear data) calculations. Recent research has led to the development of the Subgroup Decomposition Method, which resolves the spectral core environment effect by iterating between consistent condensed group criticality calculations and fixed-source decomposition sweeps, which allow the fine-group flux to be extracted from the condensed solution. This process corrects for the core environment effect and generates results which possess the accuracy of fine-group calculations without the computation time associated with direct fine-group transport. Thus far, the method has only been demonstrated in LWR and VHTR applications, and been shown to provide fine-group accuracy with significant improvements in computation time. In this paper, the method is described and its effectiveness is examined in fast reactor applications. A new 1D fast reactor benchmark problem was developed to demonstrate the new method in a discrete ordinates framework, and results were generated for eigenvalue, pin power, and fine-group angular flux using a 1-group and 6-group condensed structure. These results are compared with the results of a direct transport calculation in 112 groups. The method is shown to exactly reproduce the 112 group solution independent of the broad-group structure.

1. Introduction

One of the central difficulties of solving the neutron transport equation for large scale problems like nuclear reactors is the large memory and computational cost necessary for a sufficiently fine discretization of the phase space. Historically, this has limited whole-core analysis to nodal diffusion theory calculations with cross sections that are homogenized over entire lattice cells (e.g., fuel assemblies) and condensed to only a few broad energy groups. Recent advancements in computer capabilities has led to a resurgent interest within the nuclear industry in performing direct (fine-mesh) transport calculations at the whole-core level without spatial homogenization and with a high-order angular treatment (e.g., discrete ordinates). This has led to the development of highly parallelized transport codes with robust spatial differencing schemes in reactor and detection/shielding applications. However, these new whole-core transport applications still generally rely on multigroup cross sections which are condensed into only a few broad energy groups to reduce the complexity (as well as the computational difficulty) of the problem.

One significant challenge is that the standard method for condensing (or homogenizing) the nuclear data (cross sections) into a few energy groups relies on a flux-weighted averaging of the cross section over the broad energy intervals. However, the energy-dependent flux is the desired solution of the transport equation, and is therefore not known *a priori*. Historically, methods developers have gotten around this by using an approximate "weighting flux" which is somewhat characteristic of the spectrum. Generally, the weighting flux is selected to be the solution to a simpler transport problem, such as a single lattice cell with specular reflective boundary conditions. However, these boundary conditions often bear little resemblance to the neutron flux in the core environment. Because this incorrect flux spectrum is used to perform condensation and/or homogenization of the cross sections, a significant error (termed "core environment error") is introduced into the whole-core solution obtained with these cross sections.

While this core environment error often is masked by error cancellation when combined with assembly-level homogenization and nodal diffusion, the transition to direct whole-core transport requires a more robust approach to cross section condensation to account for spectral core environment error. Such an approach, termed the "Subgroup Decomposition (SGD) Method," has recently been developed [1], which pairs a consistent condensation method for broad-group eigenvalue calculations with a set of fixed-source transport sweeps to extract the core-level fine-group flux spectrum. This method has thus far been demonstrated and shown to be highly effective for LWR and VHTR applications. However, as a result of the increased focus on fast-spectrum reactors and the unique challenges they possess (e.g., longer mean free path, higher leakage, increased flux anisotropy, non-fissionable lattices), it is highly desirable to examine the effectiveness of the Subgroup Decomposition Method for fast reactors. The overall goal of this paper is therefore to apply the SGD method to a fast reactor problem and examine its effectiveness.

One of the difficulties in testing new methods, particularly for advanced reactor systems, is the lack of a wide variety of available benchmark problems with which to compare performance. Most available whole-core benchmarks are generally too complex to be useful in the early stages of new methods development. In fact, methods developers often are benefited by having benchmark problems which are far simpler than the eventual intended application, as a simpler benchmark problem is easier to model and better for diagnosing / debugging new methods. These simpler benchmarks must still be able to adequately represent most of the computational challenges unique to the physics of the intended problem. As a result, this paper also includes the development of a 1D benchmark which possesses the physics and challenges characteristic of fast reactor systems but which is far simpler to model than a full 3D fast reactor.

2. Subgroup Decomposition Method

The recently developed SGD method addresses the inaccuracy induced in condensed cross sections by use of an approximate "weighting flux" from a single-lattice calculation with specular reflective boundary conditions. A detailed description of the method may be found in [1]; however, a summary is presented here for the reader's benefit. The central premise of the method is to start with a guess weighting flux, condense the cross sections and perform eigenvalue calculations in a set of broad energy groups, and then perform an inverse-condensation via fixed-source sweeps to obtain an updated fine group flux. This flux is then used to generate updated core-level broad-group cross sections, which is used to perform the broad-group eigenvalue calculation again. The exact fine-group flux for the core may then be found after sufficient iterations of this procedure. The method can be broken down into three steps: (1) consistent condensed calculations, (2) fixed-source decomposition sweeps, and (3) recondensation and repeat.

2.1 Consistent Condensation

One of the most common issues with condensed group calculations is the treatment of the total collision cross section. Because the weighting flux is angularly dependent, the condensed total group cross section takes on an angular dependence, even though the fine-group total cross section is angularly independent, as in Eq. (1).

$$\sigma_g(\vec{r},\hat{\Omega}) = \frac{\int_{E_g}^{E_{g+1}} dE\sigma(\vec{r},E)\Psi(\vec{r},\hat{\Omega},E)}{\int_{E_g}^{E_{g+1}} dE\Psi(\vec{r},\hat{\Omega},E)} \tag{1}$$

Where $\sigma(\vec{r},E)$ and $\sigma_g(\vec{r},\hat{\Omega})$ are the total cross section and total group *g* cross section, and $\Psi(\vec{r},\hat{\Omega},E)$ is the angular flux at position $\vec{r}$ and energy *E*, moving in direction $\hat{\Omega}$.

In general, reactor physics codes do not admit an angularly dependent total cross section, leading programmers and methods developers to assume that the angular flux is separable in energy and angle (i.e. $\Psi(\vec{r},\hat{\Omega},E) = \phi(\vec{r},E)\,f(\hat{\Omega})$). This is clearly incorrect for a wide variety of problems, and thus the SGD Method makes use of a recently developed consistent formulation of the condensed transport equation [2] to account for the energy angle coupling, presented in Eq. (2).

$$\hat{\Omega}\cdot\nabla\Psi_g(\vec{r},\hat{\Omega}) + \sigma_g(\vec{r})\Psi_g(\vec{r},\hat{\Omega}) = S_g(\vec{r},\hat{\Omega}) - \sum_{l=0}^{\infty}\sum_{m=-l}^{l} Y_{lm}(\hat{\Omega})\delta_g^{lm}(\vec{r})\phi_g(\vec{r}) \tag{2}$$

Where

$$\delta_g^{lm}(\vec{r}) = \frac{\int_{E_{g-1}}^{E_g} dE\left(\sigma(\vec{r},E) - \sigma_g(\vec{r})\right)\phi_l^m(\vec{r},E)}{\int_{E_{g-1}}^{E_g} dE\phi(\vec{r},E)} \tag{3}$$

and $Y_{lm}(\hat{\Omega})$ are the normalized spherical harmonics. Note that the scattering is contained within the multigroup source $S_g(\vec{r},\hat{\Omega})$, as in Eq. (4).

$$\begin{aligned} S_g(\vec{r},\hat{\Omega}) = & \frac{1}{4\pi k}\int_{E_{g-1}}^{E_g} dE\chi(\vec{r},E)\sum_{g'=1}^{G}\int_{E_{g'-1}}^{E_{g'}} dE'\nu\sigma_f(\vec{r},E')\phi(\vec{r},E') \\ & + \sum_{l=0}^{\infty}\sum_{m=-l}^{l}\frac{Y_{lm}^*(\hat{\Omega})}{4\pi}\int_{E_{g-1}}^{E_g} dE\sum_{g'=1}^{G}\int_{E_{g'-1}}^{E_{g'}} dE'\sigma_{sl}(\vec{r},E'\to u)\phi_l^m(\vec{r},E') \end{aligned} \tag{4}$$

The final term in Eq. (2) is known as the "Energy Angle Coupling Correction Term" and is treated as a source correction which makes the multigroup equation consistent with the fine-group energy angle coupling. By solving Eq. (2) during each broad-group step, the exact energy-angle coupling of the fine-group solution is preserved, guaranteeing that the converged solution will be correct. See reference [2] for a more detailed description of the consistent correction for the energy-angle coupling.

2.2 Fixed-Source Decomposition

In order to decompose the flux spectrum after the coarse-group core calculation, two additional "cross sections" are computed when the cross sections are condensed:

$$R_{fc'\to h}(\vec{r}) = \chi_h(\vec{r}) \frac{\sum_{h\in c'} \nu\sigma_{fh'}(\vec{r})\phi_{h'}(\vec{r})}{\sum_{h'\in c'} \phi_{h'}(\vec{r})} \tag{5}$$

$$R_{slmc'\to h}(\vec{r}) = \frac{\sum_{h'\in c'} \sigma_{slmh'\to h}(\vec{r})\phi^m_{lh'}(\vec{r})}{\sum_{h'\in c'} \phi^m_{lh'}(\vec{r})} \tag{6}$$

It is noted that these terms are already computed during the standard condensation calculation, but discarded in favor of the coarse-group cross sections and not used by standard coarse-group transport methods. As a result, the generation of these terms adds negligible time or memory constraints to the condensation procedure. Eqs. (5) and (6) allow a new fixed-source "decomposition sweep" equation to be written for fine-group *h* where the source is a function of the coarse-group flux and eigenvalue solution, presented in Eq. (7).

$$\hat{\Omega}\cdot\nabla\Psi_h(\vec{r},\hat{\Omega}) + \sigma_h(\vec{r})\Psi_h(\vec{r},\hat{\Omega}) = \frac{1}{4\pi k}\sum_{g=1}^{G} R_{fg\to h}\phi_g(\vec{r}) + \sum_{l=0}^{\infty}\sum_{m=-l}^{l} \frac{Y^*_{lm}(\hat{\Omega})}{4\pi}\sum_{g=1}^{G} R_{slmg\to h}(\vec{r})\phi^m_{\mathrm{lg}}(\vec{r}) \tag{7}$$

Eq. (7) is referred to as a "decomposition sweep" because the eigenvalue and source have already been obtained during the broad-group calculation, and therefore Eq. (7) requires only a single transport sweep to solve for each subgroup.

2.3 Recondensation

If the exact fine-group flux solution were known ahead of time and used to condense the cross sections, the consistent coarse-group formulation and decomposition sweeps would reproduce this flux exactly, to within the convergence of the coarse-group criticality calculation. However, using an incorrect flux as a starting point means that one must iterate between broad-group eigenvalue calculations and fine-group fixed-source decomposition sweeps. These iterations are repeated until some convergence criterion has been reached to stop the calculation. It has been shown [1,2] that using the fine-group flux as a convergence parameter, while the most natural selection, does not serve as a very practical option. This is because, for a wide class of problems, small changes in the fine-group flux spectrum do not dramatically affect the reaction rate or eigenvalue. In addition, the SGD method was originally demonstrated [1] with the coarse-group total cross section used as the convergence parameter for LWR and VHTR problems. However, because of the relatively low flux in some energy groups (e.g., thermal groups in fast reactor problems), converging the thermal cross section to within a tight convergence would be a waste of resources. For the problems in this paper, therefore, the iterations are terminated when, after the *i*th iteration, the criterion $\varepsilon^{(i)}$, defined as in Equations (8)-(9) is less than some specified value.

$$\varepsilon^{(i)} = \max \frac{\left|S_h^{(i)}(\vec{r}) - S_h^{(i-1)}(\vec{r})\right|}{\sum_h \int d\vec{r} S_h^{(i-1)}(\vec{r})} \tag{8}$$

Where

$$S_h(\vec{r}) = \frac{1}{4\pi k}\sum_{g=1}^{G} R_{fg\to h}\phi_g(\vec{r}) + \int d\hat{\Omega}\sum_{l=0}^{\infty}\sum_{m=-l}^{l}\frac{Y_{lm}^*(\hat{\Omega})}{4\pi}\sum_{g=1}^{G} R_{slmg\to h}(\vec{r})\phi_{\lg}^m(\vec{r}) \quad (9)$$

3. Benchmark Development

In order to test the SGD method for fast reactor problems without the difficulties inherent in modeling a large 3D problem, a 1D version of a fast reactor benchmark has been developed. In order to generate a benchmark problem which is characteristic of the physics of fast reactors, a 3D fast reactor benchmark was selected from the available literature, and then reduced via a volume-weighted smearing of the number densities and an area-equivalent reduction from hexagonal geometry into slab geometry.

The starting point for the benchmark problem is a 3D model of the 250 MWt Advanced Burner Test Reactor (ABTR) generated by Allen et. al [3]. The ABTR is based on the GE PRISM design, with number densities specified at Equilibrium Concentration and core geometry specified at Hot Operating Condition (Fuel @ 923.15K, Structure/Coolant @ 783.15K)) [4]. In order to generate a 1D version of the hexagonal assemblies in the ABTR, an equivalent area circle is generated, with the area of each material preserved from the hexagonal model. A 1D slab is then generated which has the same width as the diameter of the equivalent circle and with the total volume of each material preserved. A visualization of this procedure is demonstrated in Fig. 1.

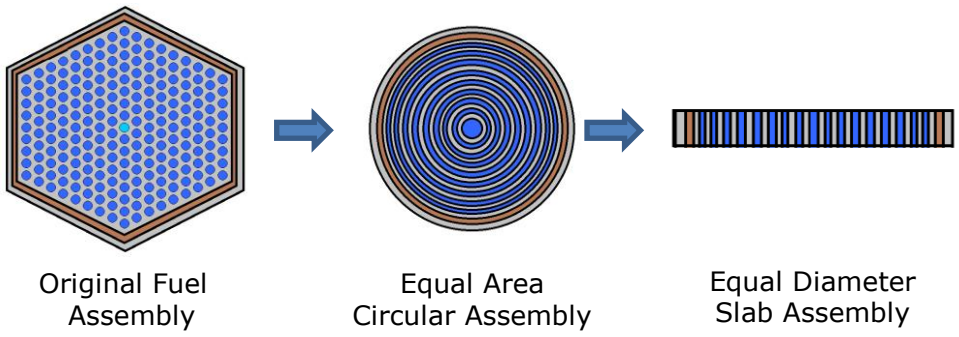

Fig 1. Reduction of Hexagonal Assembly to 1D Slab Assembly

The core layout is also treated by volume preservation. The core is broken up into a series of rings as in Fig. 2, and the width of each 1D lattice is scaled to the number of 2D lattices in that ring. The material number densities are then obtained by a volume-weighted averaging over the assemblies in the ring.

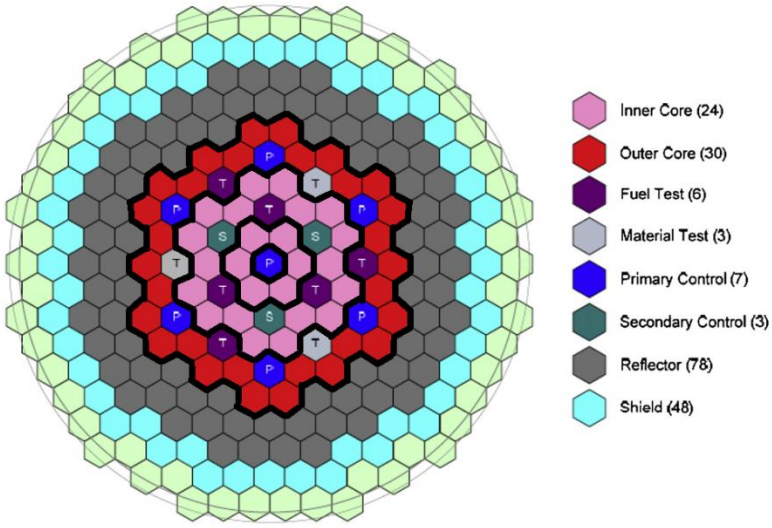

Fig 2. Ring divisions for the ABTR Core Layout

Table 1 presents the number of 2D lattices of each type (PCR = Primary Control, SCR = Secondary Control, IF = Inner Fuel, MF = Middle Fuel, OF = Outer Fuel, RF = Reflector, SH = Shield) contained within each ring, as well as the equivalent radius of a circle with the same area as the assemblies contained within that ring, as well as the assembly width in the 1D slab version of the core, presented in Fig. 3. For the purposes of this benchmark problem, the core barrel is ignored.

1D Lattice Type	PCR	SCR	IF	MF	OF	RF	SH	Total	EqR (cm)	AssW (cm)
Center Control	1							1	7.71	7.71
Inner Fuel			6					6	20.40	12.69
Mixed Assy A		3	18	3				24	42.93	22.53
Mixed Assy B	6			3	30	3		42	65.88	22.95
Reflector						78		78	94.74	28.87
Shield							48	48	108.77	14.02
Total	7	3	24	6	30	81	48	199		108.77

Tab 1: Number of each type of 2D lattice contained in each 1D lattice and geometric scaling of each 1D lattice

Fig 3. Core layout of 1D ABTR

The number density and total width of each material in the 1D problem is obtained by a volume-weighted preservation of the 2D core layout. In the Mixed Fuel A and Mixed Fuel B assemblies, the number densities of the non-fuel assemblies in the core ring are smeared into the interpin coolant within the fuel assemblies. In the event that primary and secondary control rods are inserted, the control material is smeared into this non-fuel material. The number densities for each material are specified in Table 2, and the 1D geometry is presented in Appendix A.

Isotope	Dens (at/bcm)	Isotope	Num Dens (at/bcm)		
HT9			Inner Fuel	Fuel - Mix A	Fuel - Mix B
Fe-54	4.0824E-03	U-234	1.2225E-08	1.5386E-07	1.4546E-06
Fe-56	6.4085E-02	U-235	3.2248E-05	3.2218E-05	3.1792E-05
Fe-57	1.4800E-03	U-236	2.0561E-06	2.0407E-06	1.8674E-06
Fe-58	1.9696E-04	U-238	2.0222E-02	2.0154E-02	1.9356E-02
Ni-58	2.9316E-04	Np-237	3.8387E-06	2.9137E-05	1.9291E-05
Ni-60	1.1292E-04	Pu-236	1.3918E-11	1.4159E-10	9.0788E-11
Ni-61	4.9088E-06	Pu-238	9.5854E-07	1.3751E-05	9.1258E-06
Ni-62	1.5651E-05	Pu-239	3.4991E-03	3.3356E-03	4.1293E-03
Ni-64	3.9859E-06	Pu-240	3.7398E-04	4.7600E-04	5.1362E-04
Cr-50	4.5123E-04	Pu-241	2.4534E-05	6.3075E-05	5.3615E-05
Cr-52	8.7015E-03	Pu-242	1.7542E-06	3.2816E-05	2.1800E-05
Cr-53	9.8668E-04	Am-241	1.4209E-06	3.1655E-05	2.1394E-05
Cr-54	2.4561E-04	Am-242m	2.8475E-08	8.5778E-07	5.6738E-07
Mn-55	4.6007E-04	Am-243	6.1338E-08	6.2846E-06	4.0345E-06
Mo-Nat	4.9097E-04	Cm-242	4.7083E-08	1.0910E-06	7.1977E-07
Na Coolant		Cm-243	7.4138E-10	3.5533E-08	2.3030E-08
Na	2.2272E-02	Cm-244	4.8305E-09	1.5736E-06	1.0038E-06
CR Absorber (Used in PCR)		Cm-245	1.9064E-10	1.3976E-07	8.9014E-08
C-12	4.0679E-03	Cm-246	2.6112E-12	9.6708E-09	6.1549E-09
B-10	1.6441E-02	Zr-90	3.7527E-03	3.7527E-03	3.7527E-03
B-11	6.6179E-02	Zr-91	8.1836E-04	8.1836E-04	8.1836E-04
SH Absorber (Used in SH)		Zr-92	1.2509E-03	1.2509E-03	1.2509E-03
C-12	3.7154E-03	Zr-94	1.2677E-03	1.2677E-03	1.2677E-03
B-10	1.5668E-02	Zr-96	2.0423E-04	2.0423E-04	2.0423E-04
B-11	6.3065E-02	Mo-Nat	9.7612E-04	9.5616E-04	9.6863E-04

Isotope	Num Dens (at/bcm)			
	Mix Assy A Clt Controlled	Mix Assy A Clt Uncontrolled	Mix Assy B Clt Controlled	Mix Assy B Clt Uncontrolled
Na	1.4491E-02	2.1285E-02	1.1096E-02	1.6873E-02
Fe-54	4.8886E-04	1.8089E-04	1.2515E-03	9.8956E-04
Fe-56	7.6741E-03	2.8396E-03	1.9645E-02	1.5534E-02
Fe-57	1.7723E-04	6.5578E-05	4.5369E-04	3.5875E-04
Fe-58	2.3586E-05	8.7272E-06	6.0378E-05	4.7742E-05
Ni-58	3.5105E-05	1.2990E-05	8.9868E-05	7.1061E-05
Ni-60	1.3522E-05	5.0035E-06	3.4616E-05	2.7371E-05
Ni-61	5.8782E-07	2.1751E-07	1.5048E-06	1.1899E-06
Ni-62	1.8742E-06	6.9349E-07	4.7978E-06	3.7937E-06
Ni-64	4.7731E-07	1.7661E-07	1.2219E-06	9.6617E-07
Cr-50	5.4034E-05	1.9994E-05	1.3832E-04	1.0938E-04
Cr-52	1.0420E-03	3.8556E-04	2.6674E-03	2.1092E-03
Cr-53	1.1815E-04	4.3720E-05	3.0247E-04	2.3917E-04
Cr-54	2.9411E-05	1.0883E-05	7.5292E-05	5.9535E-05
Mn-55	5.5093E-05	2.0386E-05	1.4103E-04	1.1152E-04
Mo-Nat	5.8793E-05	2.1755E-05	1.5051E-04	1.1901E-04
C-12	9.3400E-04		7.9428E-04	
B-10	3.7749E-03		3.2102E-03	
B-11	1.5195E-02		1.2922E-02	

Tab 2: Material Compositions for 1D Benchmark

In order to generate cross sections for the benchmark problem, the entire core was modeled in HELIOS version 1.10 [5]. A core calculation was performed with the 112-group HELIOS Fast Reactor library, and 112-group cross sections were output for each unique material in the core (Fuel 1, Fuel 2, Fuel 3, HT9 Steel, Sodium Coolant, Control Rod Absorber (B_4C), Shield Absorber (B_4C), Mixed Fuel Interpin Coolant A, and Mixed Fuel Interpin Coolant B).

Once cross sections were obtained, a 112-group S_8 calculation was performed with transport-corrected scattering to obtain the reference solution. For sake of brevity, only the uncontrolled configuration is examined in this paper. The reference is presented in Fig. 4 for the 112-group flux integrated into a 6-group structure (G1 – fast, G6 – thermal) on the left axis and the pin fission density (normalized to the number of pins) on the right axis. In the figure, the left boundary (specular reflective) is at position 0 cm, and the right boundary (vacuum) is at position 108.77 cm.

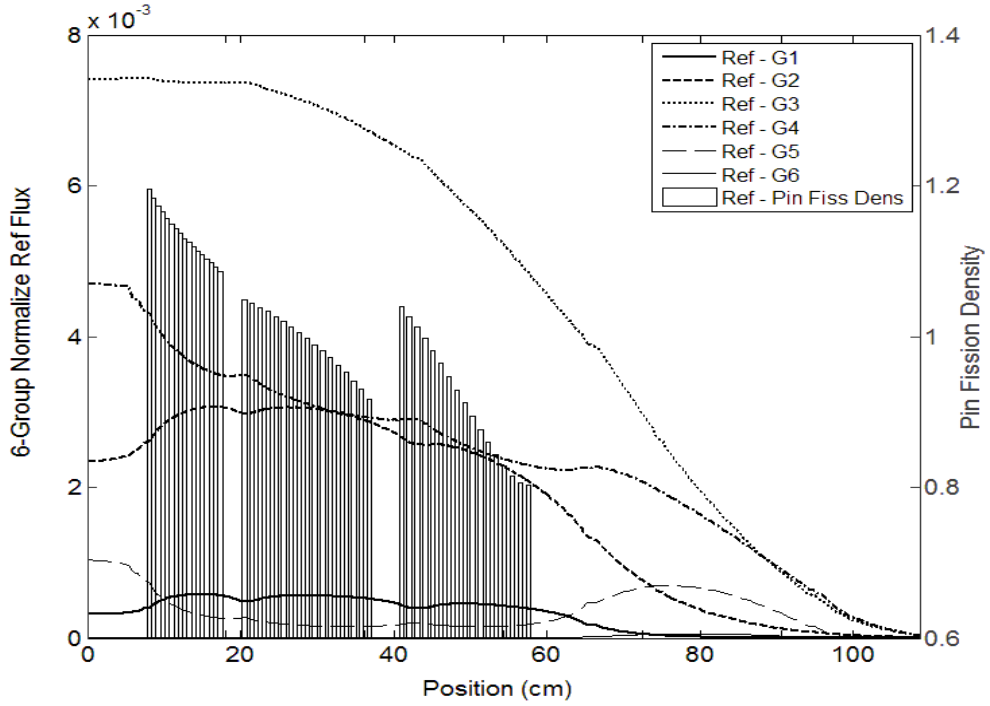

Fig 4. Reference Solution – 6-Group Flux and Pin Fission Density

4. Results

In order to determine the accuracy and efficiency of the SGD method for the 1D fast reactor, both the "standard method" (lattice cell flux used to condense the cross sections) and the SGD method (starting with the lattice cell flux as an initial guess) were used to solve the core problem in 1 and 6 groups. The SGD calculations were performed until the convergence parameter $\varepsilon^{(i)}$ was less than 10^{-4}. The results of the SGD method were then compared to the 112-group reference S_8 solution. The eigenvalue convergence results for the SGD method are presented in Table 3.

	112-g Ref	1.36708
SGD Itns	δk^*, 1-Group (pcm)	δk^*, 6-Group (pcm)
0**	3701	660
1	2266	324
2	2348	366
3	2293	386
4	2208	377

5	2117	363
10	1686	222
…	..	…
Final	-22 (225 itns)	8 (157 itns)

* $\delta k=10^5(k-k_{112g})/\ k_{112g}$
** Standard method

Tab 3: Eigenvalue Convergence of SGD Method for 1D Fast Reactor

As expected, the standard method produces error in the eigenvalue of more than 3% in the 1-group case, and while the 6-group eigenvalue is improved, it still was more than 600 pcm off. On the other hand, SGD method reproduces the 112-group eigenvalue to within 25 pcm when the fine group source is converged, independent of the number of broad groups. Figure 5 presents the flux-weighted %-error in the broad-group scalar flux and the %-error in pin fission density for the SGD and standard methods. Note that the scales on the SGD solutions (on right) and the standard method solutions (on left) are different, as the error using the SGD is too small to be seen with the standard method scale.

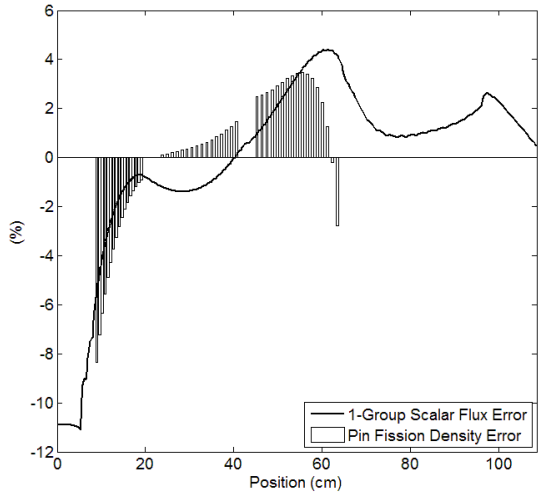

1G Standard Method

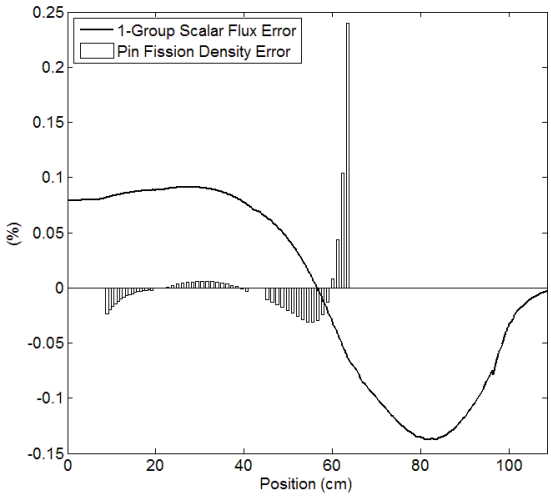

1G SGD Method

(a) 1-Group Structure

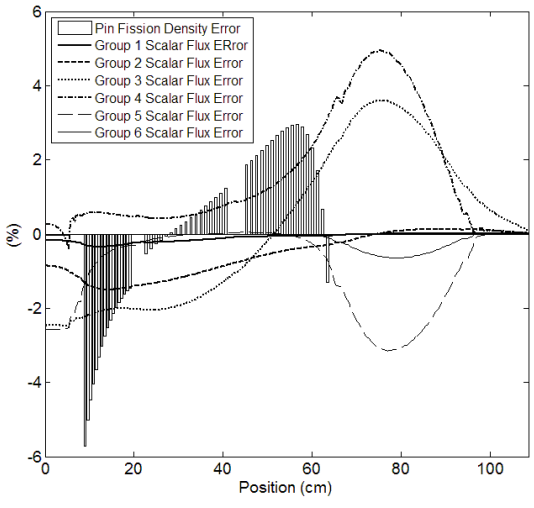

6G Standard Method

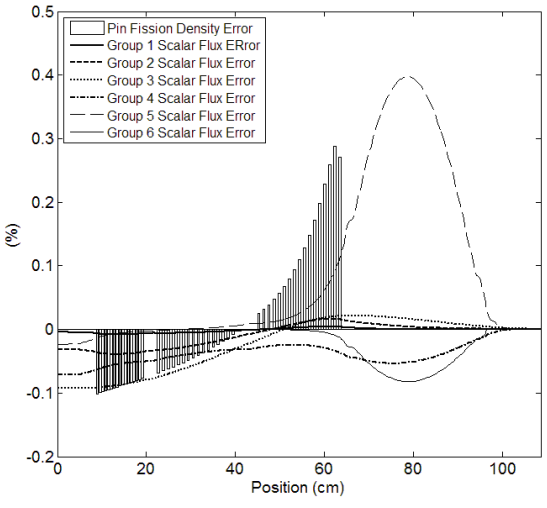

6G SGD Method

(b) 6-Group Structure

Fig. 5. Weighted %-Error in Flux and Pin-Power for 1D Fast Reactor Problem using Standard and SGD Methods in 1 and 6 Groups

As expected, the standard method results in significant errors in the pin fission density and scalar flux using either the 1-group or 6-group structure. As was demonstrated with the eigenvalue, the SGD method is able to fully correct for this, resulting in less than 0.3% error in the pin fission density. In Table 6, the error in the pin fission density calculation is presented numerically for each case and compared with the error in the standard method (lattice cell flux used to weight the cross sections). In the table, the maximum (MAX), average (AVG), root-mean-square (RMS), and flux-weighted (FWE) errors are presented.

	1-Group Standard	1-Group SGD	6-Group Standard	6-Group SGD
MAX (%)	8.3	0.24	5.7	0.29
AVG (%)	2.2	0.01	1.9	0.09
RMS (%)	2.9	0.04	2.3	0.10
FWE (%)	2.3	0.02	1.9	0.08

Tab 6: Pin Fission Density Error for 1G and 6G Calculations

As demonstrated in the table, using the lattice cell flux to weight the cross section resulted in more than 5% maximum error in the pin fission density, but by using the SGD method to correct for the inappropriate initial flux guess, this error is reduced to less than 0.3%. In general, the SGD method is shown to be able to fully correct for the large errors present in the standard method.

5. Conclusions

The results in the previous section demonstrate that the SGD method accurately reproduces the fine-group transport solution through iterative recondensation of the cross sections via decomposition sweeps. Previous work for LWR and VHTR analysis has demonstrated that, while the SGD solution is accurate, the efficiency of the method (number of required SGD iterations) is highly subject to the number of broad groups, their boundaries, and the overall physics of the problem [1]. It was demonstrated in that work that the broad-group structure had a more significant effect on VHTR problems due to the longer mean free paths, and in this work a similar effect has been seen. The most effective use of the method is to rapidly correct for strong local flux gradients across the interfaces of neighboring lattices (such as in BWR controlled bundles), and this paper has demonstrated that this can be fully accounted for using the method in fast reactors. However, the significantly reduced flux gradients and much longer mean free paths in the fast reactor problem resulted in a much slower convergence of the method than in thermal reactors. As a result, the SGD method requires an extremely large number of iterations to correct for the core environment effect in fast reactors. It is expected that the method will significantly benefit from the use of an acceleration scheme on the SGD iteration process to more efficiently handle core environments which are subject to such slow convergence. Work on implementation of such a scheme is currently in progress to improve the applicability of the method to fast reactor systems.

The results presented in this paper and in other publications on methods which correct for the core environment error [1,2,6,7] also demonstrate the need for a more detailed analysis of the effect of broad-group structure on recondensation methods and the development of an effective group structure optimization scheme for the method. Development and implementation of such a scheme, applicable to both the SGD and CGEC methods is intended as future work.

6. References

1. Douglass, S. and Rahnema, F., "Subgroup Decomposition Method," *Annals of Nuclear Energy* **48**, pgs. 84-101 (2012).
2. Douglass, S. and Rahnema, F., "Consistent Generalized Energy Condensation Theory," *Annals of Nuclear Energy* **40**, pgs. 200-214 (2012).
3. Allen, K., Knight, T., and Bays, S., "Benchmark of Advanced Burner Test Reactor Model Using MCNPX 2.6.0 and ERANOS 2.1," *Progress in Nuclear Energy* **53**, pgs. 633-644 (2011).
4. Chang, Y.I., Finck, P.J., and Grandy, C. "Advanced Burner Test Reactor Preconceptual Design Report," Technical Report, Argonne National Laboratory, *ANL-AFCI-173* (2006).
5. Simeonov, T., "Release Notes – HELIOS System Version 1.8" Studsvik Scanpower Report, SSP-03/221, (2003).
6. Douglass, S., and Rahnema, F., "Cross Section Recondensation Method via Generalized Energy Condensation Theory," *Annals of Nuclear Energy* **38**, pgs. 2105-2110 (2011).
7. Douglass, S., and Rahnema, F. "Cross Section Recondensation as Spectral Correction for Non-Fissionable Regions of VHTR Cores," *Am. Nucl. Soc. National Meeting, June 24-28, Chicago, IL* (2012).

7. Appendix A

The geometric parameters of each assembly are presented in Table A.1.

	Inner Fuel		Mixed A		Mixed B	
Assembly Width (cm)	12.69	Mat	22.53	Mat	22.95	Mat
Fuel Pin Width (cm)	0.334	Inner Fuel	0.519	Mix A Fuel	0.475	Mix B Fuel
Clad Width (cm)	0.057	HT9	0.089	HT9	0.081	HT9
Duct Width (cm)	0.497	HT9	0.882	HT9	0.898	HT9
Bypass Width (cm)	0.343	Na	0.609	Na	0.620	Na
InterPin Coolant (cm)	0.188	Na	0.428	Mix A Clt	0.504	Mix B Clt
Pin Pitch	0.637		1.125		1.142	
Number of Pins	17		17		17	
	Reflector		Shield		PCR*	
Assembly Width (cm)	28.87	Mat	14.02	Mat	15.42	Mat
Rod Width (cm)	2.007	HT9	1.466	SH	0.511	CR
Clad Width (cm)			0.317	HT9	0.084	HT9
InterRod Coolant (cm)	0.248	Na	0.278	Na	0.230	Na
Outer Duct Width (cm)	1.130	HT9	0.549	HT9	0.603	HT9
Bypass Width (cm)	0.780	Na	0.379	Na	0.417	Na
Inner Duct Width (cm)					0.764	HT9
Inter-Duct Bypass (cm)					0.764	Na
Rod Pitch	2.255		2.378		0.909	
Number of Rods	11		5		11	

Tab A.1: Geometry and Materials for slabs in 1D ABTR Benchmark
*PCR is modeled in ½ symmetry, but entire lattice geometry is presented

MEASUREMENT OF THE AM243 NEUTRON CAPTURE CROSS SECTION AT THE N_TOF FACILITY AT CERN

E. MENDOZA[1], D. CANO-OTT[1], C. GUERRERO[4,1], U. ABBONDANNO[3], G. AERTS[17], H. ÁLVAREZ[26], F. ÁLVAREZ-VELARDE[1], S. ANDRIAMONJE[4], J. ANDRZEJEWSKI[5], P. ASSIMAKOPOULOS[6], L. AUDOUIN[7], G. BADUREK[8], P. BAUMANN[9], V. BÉCARES[1], F. BECVAR[10], F. BELLONI[3], E. BERTHOUMIEUX[17], M. CALVIANI[4], F. CALVIÑO[11], R. CAPOTE[12,13], A. CARRILLO DE ALBORNOZ[14], P. CENNINI[15], V. CHEPEL[16], E. CHIAVERI[4], N. COLONNA[2], G. CORTES[18], A. COUTURE[19], J. COX[19], M. DAHLFORS[15], S. DAVID[7], I. DILLMAN[20], R. DOLFINI[21], C. DOMINGO-PARDO[22], W. DRIDI[17], I. DURAN[26], C. ELEFTHERIADIS[23], L. FERRANT[7], A. FERRARI[15], R. FERREIRA-MARQUES[16], H. FRAIS-KOELBL[12], K. FUJII[3], W. FURMAN[24], A. GARCÍA-RÍOS[1], I. GONCALVES[16], E. GONZÁLEZ-ROMERO[1], A. GOVERDOVSKI[25], F. GRAMEGNA[15], E. GRIESMAYER[12], F. GUNSING[17], B. HAAS[27], R. HAIGHT[28], M. HEIL[20], A. HERRERA-MARTINEZ[15], M. IGASHIRA[29], S. ISAEV[7], E. JERICHA[8], F. KÄPPELER[20], Y. KADI[15], D. KARADIMOS[6], D. KARAMANIS[6], M. KERVENO[9], V. KETLEROV[25], P. KOEHLER[30], V. KONOVALOV[24], E. KOSSIONIDES[31], M. KRTICKA[10], C. LAMPOUDIS[23,17], H. LEEB[8], A. LINDOTE[16], I. LOPES[16], M. LOZANO[13], S. LUKIC[9], J. MARGANIEC[5], L. MARQUES[14], S. MARRONE[2], T. MARTÍNEZ[1], C. MASSIMI[32], P. MASTINU[15], M. H. MEAZE[2], A. MENGONI[12,39], P.M. MILAZZO[3], C. MOREAU[3], M. MOSCONI[20], F. NEVES[16], H. OBERHUMMER[8], S. O'BRIEN[19], M. OSHIMA[33], J. PANCIN[17], C. PAPACHRISTODOULOU[6], C. PAPADOPOULOS[34], C. PARADELA[26], N. PATRONIS[6], A. PAVLIK[35], P. PAVLOPOULOS[36], L. PERROT[17], M.T. PIGNI[8], R. PLAG[20], A. PLOMPEN[37], A. PLUKIS[17], A. POCH[18], C. PRETEL[18], J. PRAENA[15], J. QUESADA[13], T. RAUSCHER[38], R. REIFARTH[28], M. ROSETTI[39], C. RUBBIA[21], G. RUDOLF[9], P. RULLHUSEN[37], J. SALGADO[14], L. SARCHIAPONE[15], I. SAVVIDIS[23], C. STEPHAN[7], G. TAGLIENTE[2], J.L. TAIN[22], L. TASSAN-GOT[7], L. TAVORA[14], R. TERLIZZI[2], G. VANNINI[32], P. VAZ[14], A. VENTURA[39], D. VILLAMARIN[1], V. VLACHOUDIS[4], R. VLASTOU[34], F. VOSS[20], S. WALTER[20], H. WENDLER[15], M. WIESCHER[19], K. WISSHAK[20]

(The n_TOF Collaboration (www.cern.ch/ntof))

1 Centro de Investigaciones Energética s Medioambientales y Tecnológicas CIEMAT, Madrid, Spain
2 Istituto Nazionale di Fisica Nucleare (INFN), V. Orabona 4, 70126 Bari, Italy
3 Istituto Nazionale di Fisica Nucleare (INFN), Trieste, Italy
4 CERN, Geneva, Switzerland
5 University of Lodz, Lodz, Poland
6 University of Ioannina, Greece

7 Centre National de la Recherche Scientifique/IN2P3 - IPN, Orsay, France
8 Atominstitut der Österreichischen Universitäten,Techn. Universität Wien, Austria
9 Centre National de la Recherche Scientifique/IN2P3 - IReS, Strasbourg, France
10 Charles University, Prague, Czech Republic
11 Universidad Politécnica de Madrid, Spain
12 International Atomic Energy Agency (IAEA), Nuclear Data Sect., Vienna, Austria
13 Universidad de Sevilla, Spain
14 Instituto Tecnologico e Nuclear (ITN), Lisbon, Portugal
15 Istituto Nazionale di Fisica Nucleare (INFN), Laboratori Nazionali di Legnaro, Italy
16 LIP - Coimbra & Departamento de Fisica da Universidade de Coimbra, Portugal
17 CEA/Saclay - DSM/DAPNIA, Gif-sur-Yvette, France
18 Universitat Politecnica de Catalunya, Barcelona, Spain
19 University of Notre Dame, Notre Dame, USA
20 Forschungszentrum Karlsruhe GmbH (FZK), Institut für Kernphysik, Germany
21 Università degli Studi Pavia, Pavia, Italy
22 Instituto de Fısica Corpuscular, CSIC-Universidad de Valencia, Spain
23 Aristotle University of Thessaloniki, Greece
24 Joint Institute for Nuclear Research, Frank Lab. Neutron Physics, Dubna, Russia
25 Institute of Physics and Power Engineering, Kaluga region, Obninsk, Russia
26 Universidade de Santiago de Compostela, Spain
27 Centre National de la Recherche Scientifique/IN2P3 - CENBG, Bordeaux, France
28 Los Alamos National Laboratory, New Mexico, USA
29 Tokyo Institute of Technology, Tokyo, Japan
30 Oak Ridge National Laboratory, Physics Div ision, Oak Ridge, USA
31 NCSR, Athens, Greece
32 Dipartimento di Fisica, Università di Bologna, and Sezione INFN di Bologna, Italy
33 Japan Atomic Energy Research Institute, Tokai-mura, Japan
34 National Technical University of Athens, Greece
35 Institut für Isotopenforschung und Kernphysik, Universität Wien, Austria
36 Póle Universitaire Léonard de Vinci, Paris La Défense, France
37 CEC-JRC-IRMM, Geel, Belgium
38 Department of Physics and Astronomy - University of Basel, Basel, Switzerland
39 ENEA, Bologna, Italy

ABSTRACT

New experimental data are needed to improve the design and the analysis of the performance of new nuclear reactors, as well as the investigations on the management of the spent fuel. For this reason, a large number of neutron cross section measurements of minor actinides are being performed nowadays in order to reduce the uncertainty of the evaluated cross section data. The ^{243}Am(n,γ) cross section was measured at the n_TOF facility at CERN with a BaF_2 Total Absorption Calorimeter in the energy range from 0.7 eV to 2.5 keV. The data analysis has been recently finalized, including the resonance analysis, and the results will contribute to the improvement of the accuracy of the ^{243}Am neutron cross section.

1. **Introduction**

Nuclear data for minor actinides are necessary for improving the design and performance of advanced reactors and transmutation devices for the incineration of radioactive nuclear waste. In particular, the neutron capture reaction on ^{243}Am is the main “gate” to the production of most Cm and heavier isotopes in the spent fuel. Most of the ^{244}Cm created in a nuclear reactor comes

from the beta decay of ^{244}Am, which is originated by the ^{243}Am(n,γ) reaction. Isotopes heavier than ^{244}Cm are created necessarily by successive neutron capture reactions and decays starting from ^{244}Cm.
At present, there is no published neutron capture measurement of ^{243}Am below 250 eV, and all the existing evaluations of the elastic and capture cross sections are based essentially on a single transmission measurement made by Simpson et al. [1] in 1974. Above 250 eV there are only a few capture measurements available [2],[3], which show discrepancies that make them incompatible. Due to the lack of experimental data on ^{243}Am the standard ENDF format libraries, such as ENDF/B, JEFF or JENDL, present sizable differences between each other.
The results of the detailed analysis of this measurement, which contribute to reduce the current ^{243}Am capture cross section uncertainty, will be published soon; and the measured yield will be included in the EXFOR data base.

2. **The cross section measurement**

The ^{243}Am neutron capture cross section was measured in the 0.7 eV – 2.5 keV energy range at the n_TOF facility [4] during the 2004 campaign. This measurement was performed with the n_TOF Total Absorption Calorimeter [5] (TAC), which is composed by 40 BaF_2 crystals covering almost the entire solid angle. The high segmentation of the TAC and its high geometric and intrinsic efficiencies make it an excellent device for measuring low mass and/or radioactive samples.
The ^{243}Am sample was placed in the center of the TAC and the capture reactions were measured by detecting in coincidence the electromagnetic cascades following the neutron capture. The detector signals were recorded by a digital data acquisition system [7] operating at 250 MSamples/s with 8 bits resolution, recording continuously a time of flight of 8 ms for each pulse. The neutron energy was obtained by the time of flight technique. Some conditions on the energy and multiplicities of the detected events were applied in order to obtain a good signal to background ratio without loosing much detection efficiency, which was obtained by Monte Carlo calculations [6]. The background was obtained by dedicated measurements. A detailed description of a similar analysis procedure can be found in [8]. However, two additional difficulties were found with respect to previous measurements with the TAC at n_TOF:

1. The very high counting rate detected by the TAC due to the sample activity of 5.4 counts/μs, the highest measured up to now at n_TOF. This high counting rate induced changes in the gain of the BaF_2 detectors and enhances dead time effects in the detected ^{243}Am capture and background events. New methods have been developed to deal with these effects without affecting significantly the final cross section uncertainty.
2. The ^{243}Am sample had a high purity content, founding only about 0.048 mg of ^{241}Am and 0.0025 mg of ^{240}Pu. However, the certified mass of the sample (10 mg) did not agree with a spectroscopic characterization of the sample performed at CERN, which gave a mass of 7.1 (±15%) mg. For this reason, a detailed Monte Carlo simulation of the sample activity detected by the TAC was performed, giving a mass of 6.7 (±15%) mg, thus confirming the results of the spectroscopic measurement. The analysis of the time of flight data was finally performed by normalizing the n_TOF measured capture cross section to the transmission data of Simpson et al. [1] at low neutron energies (3 – 50 eV), obtaining a final sample mass of 6.23 (±3%) mg, in agreement with the spectroscopic measurements. With this normalization, the n_TOF capture data is totally compatible with one of the two published capture data in the 0.25 – 2.5 keV energy region [2]. It was also found that the sample has inhomogeneities. This fact made impossible the analysis of the biggest ^{243}Am resonance at 1.35 eV, the only one affected significantly by shelf shielding and multiple scattering effects.

3. **Analysis results**

3.1. **Resolved Resonance Region**

The n_TOF measurement was analyzed with the SAMMY [9] code, extending the Resolved Resonance Region (RRR) up to 400 eV thanks to high energy resolution and statistics of the present measurement. Excluding the fission widths, which have no visible effect in the calculation of the elastic and capture cross sections of ^{243}Am, all the present standard ENDF format libraries adopt the evaluations performed by Mughabghab (ENDF-VII.1), Weston (ENDF-VII.0) and Maslov (rest of the libraries) in the RRR, being the evaluations performed by Mughabghab and Weston very close to each other. In the comparison between the n_TOF results and the present evaluations it was found that:

1. The RRR in the present evaluations extends up to 250 eV, with 218 resonances (Mughabghab and Weston) and 238 resonances (Maslov). The n_TOF evaluation contains 248 resonances up to 250 eV and 105 new resonances between 250 and 400 eV.
2. The n_TOF results are, in general, in good agreement with the present evaluations up to 70 – 80 eV, with the exception of the stronger resonances, where it seems that the Maslov evaluation overestimate the shelf-shielding and multiple scattering effects. Above this energy the differences increase. An example is given in Fig 1, where the capture yield in the sample has been displayed together with the resulting theoretical capture yields obtained from the different cross section evaluations.

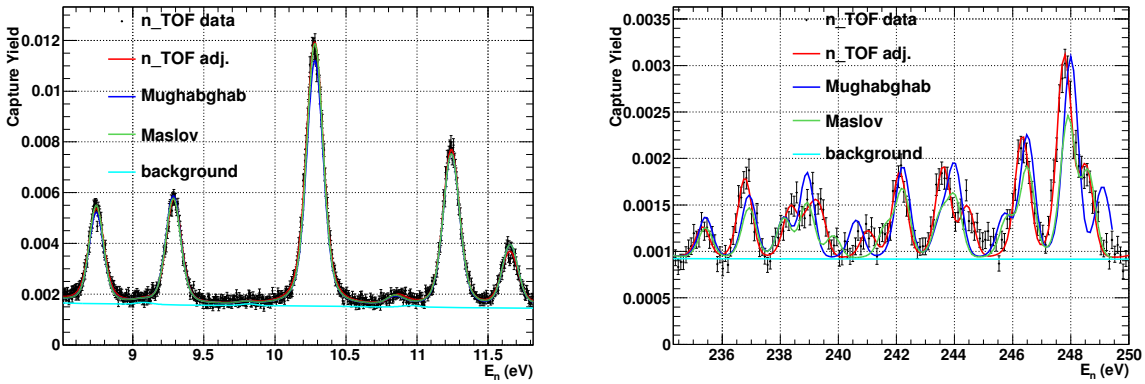

Fig 1. Adjustment of the n_TOF data compared with other present evaluations.

3. The n_TOF capture cross section is, on average, 6% larger than the Mughabghab and Weston evaluations and 13% larger than the Maslov evaluation. However, these values are not constant in the full energy range, as it is presented in Fig 2, were the capture cross sections have been averaged in intervals of 50 eV width and differences as large as 25% are found.
4. The n_TOF elastic cross section is, on average, a 3% smaller than the Mughabghab and Weston evaluations and a 7% larger than the Maslov evaluation. Again, these values are not constant in the full energy range, as it is presented in Fig 3.

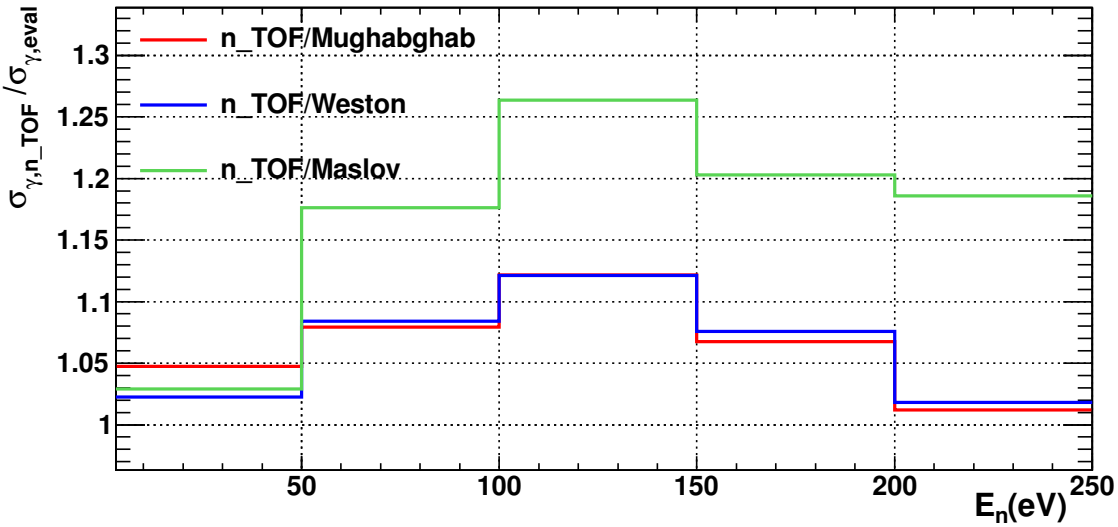

Fig 2. Comparison between the n_TOF adjusted capture cross section and the Mughabghab (ENDF/B-VII.1), Weston (ENDF/B-VII.0, ENDF/B-VI) and Maslov (latest versions of JEFF, JENDL, BROND and CENDL libraries) evaluations. The lower limit of the first bin is 3 eV.

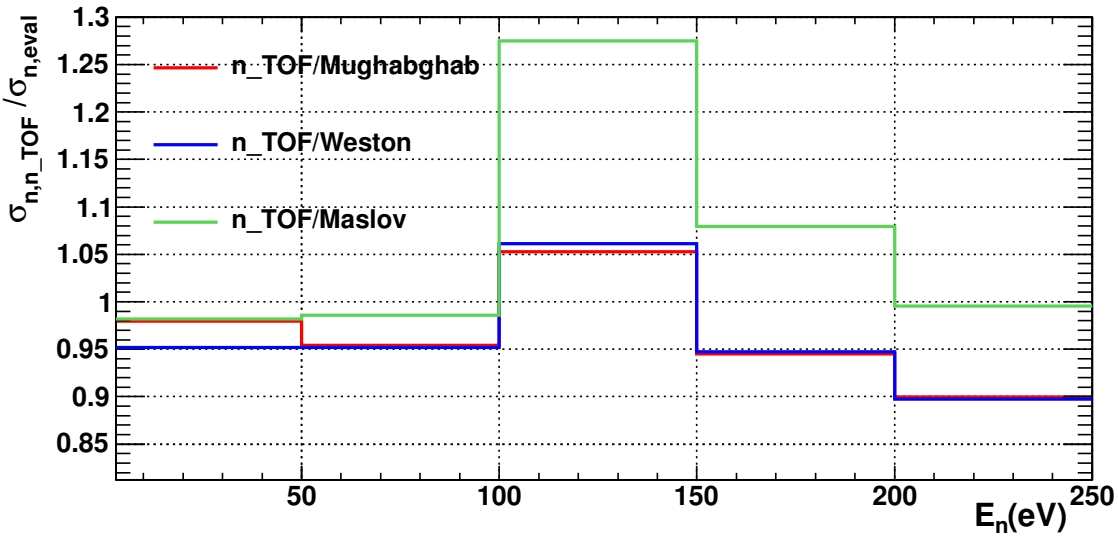

Fig 3. Comparison between the n_TOF adjusted elastic cross section and the Mughabghab (ENDF/B-VII.1), Weston (ENDF/B-VII.0, ENDF/B-VI) and Maslov (latest versions of JEFF, JENDL, BROND and CENDL libraries) evaluations. The lower limit of the first bin is 3 eV.

3.2. **Unresolved Resonance Region**

In all the recent evaluations, the ^{243}Am Unresolved Resonance Region (URR) goes from 250 eV up to 40 – 42 keV, which is the threshold for the first inelastic channel of ^{243}Am. The n_TOF data range only up to 2.5 keV, and up to 5 keV there are only two published measurements, both performed by Weston et al. [2] in 1985. The data presented in Fig 4 shows that the n_TOF results are compatible with the "Weston I" data but not with the "Weston II" data, whereas the current standard ENDF format libraries are in better agreement with the "Weston II" data. This is an important check for the reliability of the n_TOF capture data normalization and indicates that the present evaluations should be increased between 10% and 20% in the URR energy range up to 250 eV.

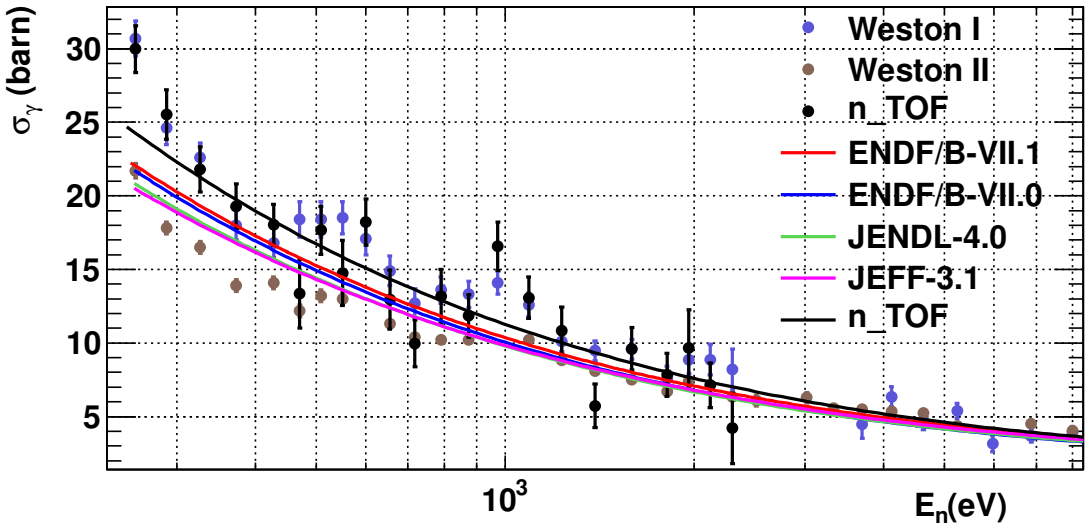

Fig 4. n_TOF data in the low energy part of the URR, together with the only two published ^{243}Am capture data below 5 keV, "Weston I" and "Weston II" , and the main current evaluations (JEFF3.1 is the same as JEFF3.2, JENDL3.3 and CENDL3.1).

3.3. **Analysis above 2.5 keV**

There is another ^{243}Am capture measurement between 5 and 250 keV, performed by Wisshak et al. [3]. This latter measurement is between 10% and 15% lower than the Weston cross section. Since the n_TOF data is in good agreement with the Weston results it seems reasonable to use the Weston results for the analysis instead of the Wisshak data.

The analysis of the complete URR can be performed by using the n_TOF data up to 2.5 keV and the Weston data (see Fig 4) between 2.5 and 42 keV. In this later energy range both Weston data sets are compatible. The ratio between the result of this analysis and the main current evaluations is presented in Fig 5, where sizeable differences between libraries can be appreciated. The trend with the neutron energy of the URR cross section obtained in this work is quite similar to that of the ENDF/B-VII.0 evaluated library, but a 10–12 % higher. With respect to other libraries, they are ~10-20% lower than the present results at 300 eV and as much as 10% lower (ENDF/B-VII.1) at 40 keV.

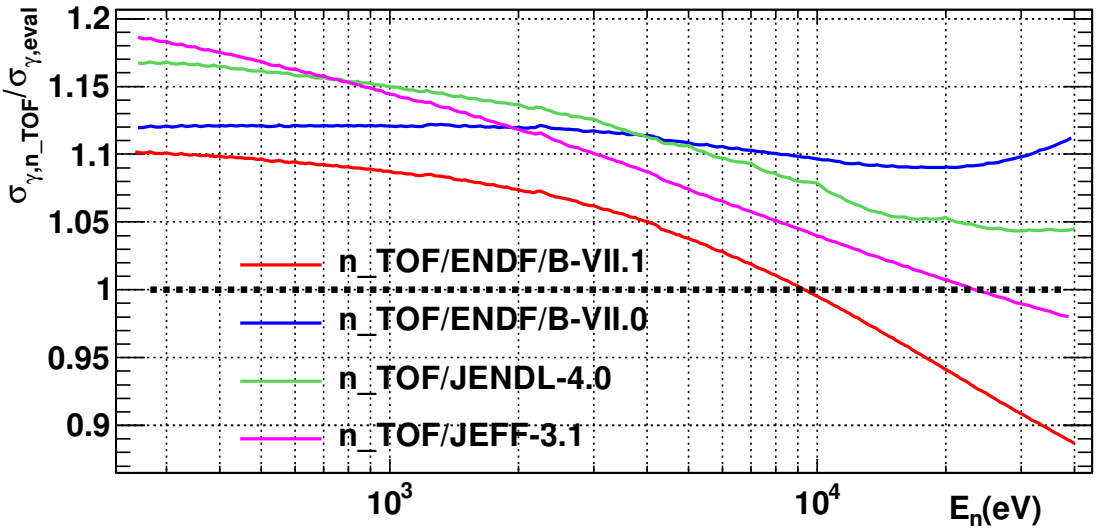

Fig 5. Ratio between the n_TOF + Weston analysis results and the main current evaluations (JEFF3.1 is the same as JEFF3.2, JENDL3.3 and CENDL3.1).

Apart from the differential measurements of Weston and Wisshak, there are some integral capture measurements that can be considered. One of these experiments is the PROFIL-1 irradiation experiment, where an ^{243}Am sample were irradiated in the fast PHENIX reactor in 1974 [10],[11]. Indeed, the changes in the ENDF/B-VII.1 evaluated library with respect with to ENDF/B-VII.0 were motivated from the results of this integral experiment [12]. The information which can be obtained from this experiment is the ^{243}Am effective capture cross section, i.e., the integral of the neutron flux convoluted with the capture cross section over the entire neutron energy range.

It has been possible to obtain a simulated flux of the PHENIX reactor at the sample position and compare the experimental values of PROFIL-1 with calculations using the capture cross section from this work. The latter has been completed, above 42 keV, with all the available evaluations. The results of this comparison are shown in Table 1, where the comparison is expressed as the ratio of the calculated to the experimental integral ratios (C/E).

Library used for E_n>42keV	C/E	Library used for E_n>42keV	C/E
ENDF/B-VII.1	0.939	JEFF-3.0	0.959
ENDF/B-VII.0 (=VI.8)	0.889	CENDL-3.1	0.947
JENDL-4.0	0.904	ROSFOND-2010	0.860
JEFF-3.1 (= JENDL3.3)	0.929	ENDF/B-V.0	0.730

Table 1 . Calculated to experimental integral capture values obtained with the cross section obtained in this work up to 42 keV and the evaluated cross sections above 42 keV.

The experimental uncertainty of the PROFIL-1 integral value is 5%, which makes the high energy regions of the ENDF/B-VII.0, JENDL-4.0, ROSFOND-2010 and ENDF/B-V.0 incompatible with the PROFIL-1 results.

In addition, the high energy region of ENDF/B-VII.1 presents a large discontinuity at 42 keV with respect to the present result. Furthermore, the JEFF-3.0 evaluation does not reproduce the Wisshak data above 42 keV when the Wisshak data are renormalized to the Weston ones. This renormalization has sense since the n_TOF and the Weston data are in good agreement and because it is not possible to reproduce the Wisshak data and the PROFIL-1 experiment at the same time. For all these reasons, the present analysis indicates that the better results are obtained with the high energy capture cross sections of the JEFF-3.1 (same as JENDL-3.3) and CENDL-3.1 libraries.

Thus, it can be concluded that the ^{243}Am capture cross section obtained from the RRR and URR of this work up to 42 keV and the JEFF-3.1 or the CENDL-3.1 evaluations above 42 keV: (1) fits the n_TOF data between 0.7 eV and 2.5 keV; (2) fits the "Weston I" data between 0.25 and 2.5 keV; (3) fits both Weston data sets between 2.5 keV and 42 keV; (4) fits the Wisshak data up to 250 keV, if they are normalized to the Weston data; (5) is compatible with the integral experimental results of the PROFIL-1 irradiation experiment; and (6) there is a continuous matching between the URR and the high energy region, at 42 keV.

4. **Conclusions**

The ^{243}Am capture cross section has been measured at n_TOF using the BaF_2 Total Absorption Calorimeter in the energy range between 0.7 eV and 2.5 keV. The analysis of the measurement has been recently finished.

Due to the large flight path of the n_TOF facility and the statistics achieved, the results provide a better description of the resolved resonance parameters, excluding the fission widths and the biggest ^{243}Am resonance at 1.35 eV, than the ones available in the current evaluated libraries, which are based essentially in one single transmission experiment. The uncertainty in the resonance parameters have been reduced, new resonances have been found and the resolved resonance region has been extended from 250 eV up to 400 eV.

Concerning the unresolved resonance region, it has been found that the n_TOF results are compatible with one of the two published capture measurements in the 0.25–2.5 keV energy region. Due to the fact that the current evaluations are closer to the other capture measurement, they underestimate the ^{243}Am cross section by 10–20 % in the mentioned energy range.

Finally, other measurements have been used to analyze the ^{243}Am capture cross section beyond 2.5 keV, finding the result that better reproduces the measurements performed up to now, including both differential and integral measurements.

5. **Acknowledgments**

This work has been supported by ENRESA under the CIEMAT-ENRESA agreement on "Transmutation of high level radioactive waste", by the Spanish Plan on Nuclear and Particle Physics of the Spanish Ministry of Science and Innovation (project FPA2005-06918-C03-01), the European Commission 6th Framework Programme project IP-EUROTRANS (F16W-CT-2004-516520) and the CONSOLIDER-INGENIO project CSD-2007-00042.

6. **References**

[1] O. D. Simpson et al., *Nucl. Sci. Eng.* 55, 273 (1974).
[2] L. W. Weston, J. H. Todd, *Nucl.Sci.Eng.* 91, 444 (1985).
[3] K. Wisshak and G. Käppeler, *Nucl. Sci. Eng.* 85, 251-260 (1983).
[4] The n_TOF Collaboration, *CERN INTC*-2002-037 (2003).
[5] C. Guerrero et al., *Nucl. Inst. And Meth.,* A608, 424-433 (2009).
[6] C. Guerrero et al., *Nucl. Inst. And Meth.,* A671, 108-117 (2012).
[7] U. Abbondano et al., *Nucl. Inst. And Meth.,* A538, 692-702 (2005).
[8] C. Guerrero et al., *Phys. Rev. C* 85, 044616 (2012).
[9] N. M. Larsson, *ORNL/TM*-9179/R7 (2006).
[10] G. Palmiotti et al., *AIP Conf. Proc.* 769, 1436 (2005).
[11] A. C. Kahler et al., *Nucl. Data Sheets* 112, 2997-3036 (2011).
[12] M. B. Chadwick, *Nucl. Data Sheets* 112, 2887-2996 (2011).

ELECTRA CORE DYNAMICS AND STABILITY ANALYSES

S. BORTOT, E. SUVDANTSETSEG, J. WALLENIUS
Reactor Physics Division, Royal Institute of Technology (KTH)
Roslagstullsbacken 21, 10691 Stockholm - Sweden

A. DELLA BONA
Dipartimento di Elettronica e Informazione, Politecnico di Milano
Via Camillio Golgi 40, 20133 Milano - Italy

S. LORENZI
Department of Energy, Nuclear Engineering Division – CeSNEF, Politecnico di Milano
Via La Masa 34, 20156 Milano - Italy

ABSTRACT

An analytical model has been developed to study the core dynamic performance and stability of the European Lead Cooled Training Reactor (ELECTRA). A dedicated dynamics simulation tool solving simultaneously time-dependent equations for neutronics and thermal-hydraulics has been developed based on point kinetics for the former physics and on a lumped-parameter formulation of energy and momentum balances for the latter. Constitutive equations have been linearized around different working conditions so as to enable Linear Time-Invariant (LTI) analysis tools to be employed to investigate the core stability on the entire power range and to assess the impact of uncertainties affecting the Doppler coefficient. The reactor dynamic response has been studied against such fundamental neutronics parameter by simulating three typical design-basis transient scenarios initiated by a partial control drum rotation, by an undesired increase of core pressure drop, and by an enhancement of the coolant core inlet temperature.

1. Introduction

A zero-dimensional model has been developed to study the core stability and dynamics of the European Lead Cooled Training Reactor (ELECTRA).

This reactor concept is being developed at the Royal Institute of Technology (KTH) in Sweden, and consists in a low-power (0.5 MW_{th}) fast neutron reactor operating under natural circulation of the lead coolant mainly intended for demonstration and educational purposes [1, 2].

One of the most important issues of natural circulation is the achievement of stable flow. In fact, the good natural convection capability of lead - and metal coolants in general - can be made ineffective by an unstable-regime flow behaviour due to perturbations inducing oscillations of the lead free surfaces in the reactor. In fact, under these circumstances the mass flow rate through the core may oscillate and decrease to the limit of flow reversal, causing fuel and cladding temperatures to transiently increase to significantly high values. In addition, a system like ELECTRA is more tightly coupled than a forced convection reactor both at a physics level (*i.e.*, neutronics, thermal-hydraulics) and at a component level (*i.e.*, core, heat exchanger, primary system layout), since neutronics and thermal-hydraulics undergo strong mutual feedbacks, as well as the core behaviour is influenced by the heat exchange conditions in the Steam Generator (SG). Therefore, the study of stability is to be extended to the overall coupled system, and not limited to the thermal-hydraulics area, as the feedbacks due to any non-nominal power generation within the core cannot be disregarded.

A reliable simulation tool has been recognized to be necessary in order to deeply understand these phenomena and to confirm the numerical code calculations [2]. Thus, a theoretical model of ELECTRA has been developed based on point-kinetics for neutronics, energy balances for thermal-hydraulics and momentum balance for natural circulation of the primary coolant. Such a choice has been made with the main goals of (*i*) evaluating the core stability on the entire power range and (*ii*) assessing the impact of uncertainties affecting the Doppler coefficient - whose calculated nominal value at full power is approximately zero, making ELECTRA lack a prompt negative reactivity feedback -, thanks to the possibility of linearizing the constitutive equations around different working conditions and using the Linear Time-Invariant (LTI) analysis tools.
Design-basis transient scenarios have been simulated to get some insights about the system dynamic behaviour. In particular, perturbations of the nominal state initiated by a control drum partial rotation, by an accidental increase of core pressure drop (with consequent undesired variation of lead mass flow rate), and by an enhancement of the coolant core inlet temperature (ensuing, for instance, from a variation of conditions on the SG side) have been studied.

2. Reference system description

ELECTRA primary system layout is shown in Figure 1. It consists in a pool-type reactor in which the power produced in the core is transferred to eight SGs by natural circulation of the coolant. In particular, the lead flow enters the core through an open region to be collected in a plenum and then delivered to the SGs, where it is cooled before entering the cold pool through the cold leg (located in the annular space between the reactor vessel and the cylindrical inner vessel) and returning finally to the core. All the primary components are installed inside the reactor vessel, which is shaped as a cylinder with hemispherical bottom head and flat roof.

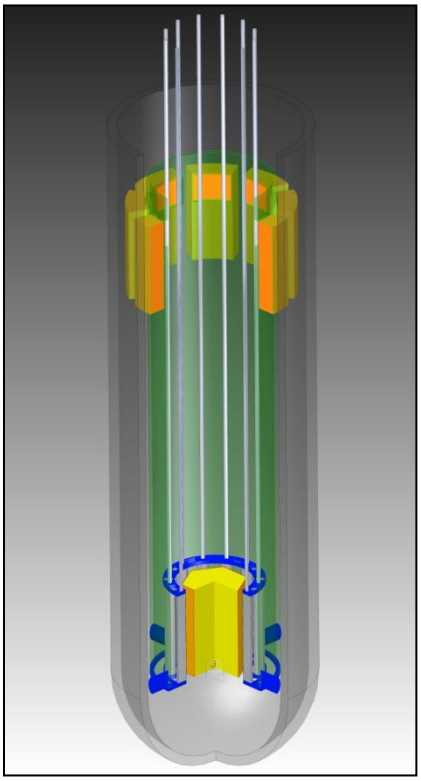

Fig 1. ELECTRA reactor block elevation

In the present paper only the core has been considered for preliminary stability and transient analyses. ELECTRA features a 0.5 MW_{th} $(Pu_{0.4}, Zr_{0.6})N$ fuelled core composed by a single wrapped hexagonal Fuel Assembly (FA) containing 397 pins on a triangular lattice. Full details concerning the referred reactor configuration can be found in [2]. ELECTRA reactivity feedback coefficients and main kinetic parameters at Beginning of Life (BoL) are displayed in Table 1.

Parameter	Value	Units
Doppler constant	-6 ± 3	pcm
Lead density coefficient (core)	-0.43 ± 0.03	pcm K^{-1}
Lead density coefficient (global)	-1.84 ± 0.04	pcm K^{-1}
Axial expansion coefficient	-0.41 ± 0.04	pcm K^{-1}
Radial expansion coefficient	-1.54 ± 0.04	pcm K^{-1}
Effective delayed neutron fraction	268 ± 1	pcm
Reactor lifetime	$0.43 \cdot 10^{-7} \pm 0.3 \cdot 10^{-8}$	s

Tab 1. ELECTRA reactivity feedback coefficients and kinetic parameters at BoL

It is noticed that all the reactivity feedbacks are negative as a consequence of the extremely compact core configuration (30 cm active height, ~15 cm equivalent active radius): the coolant density, fuel axial and, in particular, radial expansion coefficients are quite sizable, whereas the very hard neutron spectrum leads to a negligible Doppler constant. Therefore, even if the absence of positive feedback mechanisms relaxes the need for a strong Doppler effect, the impact of uncertainties affecting this safety parameter on the core stability and transient behaviour has been chosen to be further investigated.

3. Integral equation model

An analytical zero-dimensional model has been implemented incorporating a point-wise kinetics description for neutronics coupled with a single-channel, average-temperature heat transfer treatment for thermal-hydraulics. The simulator has been realized in the MATLAB/SIMULINK® environment [3].

3.1 Neutronics

Point-wise kinetics with one neutron energy group and six delayed neutron precursor groups has been employed for the core neutronics model, in which the total power is considered as generated only by fission events, the contribution of decay heat being neglected:

$$\frac{dn(t)}{dt} = \frac{\rho(t)-\beta}{\Lambda} n(t) + \sum_{i=1}^{6} \lambda_i c_i(t) \quad (1)$$

$$\frac{dc_i(t)}{dt} = \frac{\beta_i}{\Lambda} n(t) - \lambda_i c_i(t) \quad (2)$$

3.2 Thermal-hydraulics

A zero-dimensional approach has been adopted to treat also the core thermal-hydraulics. A single-node heat transfer model has been implemented by accounting of four distinct temperature regions corresponding to fuel, helium gap, cladding and coolant; in this way the reactivity feedback is enabled to include all the major contributions as well as the margins against technological limits to be monitored. In line with the point model concept, the latter temperatures have been assumed to be functions separable in space and time.

$$M_f C_f \frac{dT_f^{centr}(t)}{dt} = q(t) - k_f(T_f^{centr} - T_f^{surf}(t)), \text{ where } \frac{n(t)}{n_0} = \frac{q(t)}{q_0} \quad (3)$$

$$M_g C_g \frac{dT_f^{surf}(t)}{dt} = k_f \left(T_f^{centr} - T_f^{surf}(t)\right) - k_g \left(T_f^{surf} - T_c^{int}(t)\right) \quad (4)$$

$$M_c C_c \frac{dT_c^{int}(t)}{dt} = k_g \left(T_f^{surf}(t) - T_c^{int}(t)\right) - k_c \left(T_c^{int}(t) - T_c^{surf}(t)\right) \quad (5)$$

$$M_c C_c \frac{dT_c^{surf}(t)}{dt} = k_c \left(T_c^{int}(t) - T_c^{surf}(t)\right) - h_{cl} \left(T_c^{surf}(t) - T_l(t)\right) \quad (6)$$

$$M_l C_l \frac{dT_l(t)}{dt} = h_{cl} \left(T_c^{surf}(t) - T_l(t)\right) - \Gamma(t) C_l \left(T_l^{out}(t) - T_l^{in}(t)\right) \quad (7)$$

This separate, multi-zone pin model accounting of the temperature distribution from the fuel centerline to the coolant bulk has been employed to calculate global heat transfer coefficients: physical properties and thermal resistances have been assumed constant with temperature and time, and thermal diffusion in the axial direction within the fuel pin has been neglected.
Natural circulation of the coolant has been treated by applying the integral momentum balance over the core zone as follows:

$$\frac{L}{A}\frac{d\Gamma(t)}{dt} + P_{out} - P_{in} + \bar{d} g L + \Delta P_{loss} + \Delta P_{acc} = 0 \quad (8)$$

Accelerative pressure losses (ΔP_{acc}) have been disregarded, assuming coolant inlet and outlet velocities constant since lead is single phase. Pressure losses have been taken into account by introducing the following relationship:

$$\Delta P_{loss} = \frac{\Gamma|\Gamma|}{2\bar{d}A^2} K_c \quad (9)$$

in which the total pressure loss coefficient K_c, reckoning with form and friction effects, has been calculated by combining Rehme's model for the friction factor in wire-wrapped fuel bundles and two correlations for the friction coefficients for the FA inlet and outlet regions [4]. In order to consider the variation of K_c during transients, a correlation has been employed to express K_c as a function of mass flow rate:

$$K_c = a \cdot \Gamma^b \quad (10)$$

(with *a* and *b* being two suitable constants) so as to exploit the steady-state condition:

$$K_{c_0} \Gamma_0^{-b} = K_c \Gamma^{-b} \quad (11)$$

and to rewrite Eq. (8) as follows:

$$\frac{d\Gamma(t)}{dt} = -\frac{A}{L}\left\{\frac{\Gamma|\Gamma|^{1+b}|\Gamma_0|^{-b}K_{c,0}}{A^2 d_{in}\left[2-\delta\left(T_{l,out}-T_{l,in}\right)\right]} - d_{in} g \delta \frac{Z}{2}\left(T_{l,out} - T_{l,in}\right)\right\} \quad (12)$$

where core inlet and outlet pressures have been expressed by using the steady-state Bernoulli equation in which the levels of the hot and cold pools have been postulated to be constant in time, and the Boussinesq approximation has been applied.

3.3 Reactivity

Consistently with the lumped parameter modelling employed, the reactivity feedback has been expressed as a function of the average values of fuel and coolant temperatures, while externally introduced reactivity associated with the rotational angle of a representative control drum has

been handled as a simple input parameter. A linear relation for core expansions (axial and radial) and coolant density reactivity effects has been adopted, leading to the following expression incorporating constant coefficients:

$$\rho(t) = k_D \left(\ln \frac{T_f^{eff}(t)}{T_{f,0}^{eff}} \right) + \alpha_Z \left(T_f^{mid}(t) - T_{f,0}^{mid} \right) + (\alpha_R + \alpha_L)\left(T_l(t) - T_{l,0} \right) + \rho_{drum}(t) \quad (13)$$

As far as the Doppler effect determination is concerned, an effective average fuel temperature accounting of resonances broadening has been adopted.

4. Stability analysis

The analytical zero-dimensional model presented above is characterized by strong non-linearities, in particular as far as Eq. (12) is concerned. Consequently, the constitutive equations have been necessarily linearized to enable the use of the linear analysis theory to obtain qualitative insights into the dynamic response characteristics of ELECTRA and to verify its stability on the entire power range through calculation of the system eigenvalues (bounded-input bounded-output open-loop stability study). Moreover, the system stability has been investigated against variations of the Doppler constant calculated value in order to ensure the reactor operates under stable conditions even in case it resulted positive.

4.1 Method

According to the linear analysis theory, the dynamic behaviour of a linear system depends on the eigenvalues of the state matrix. This principle is still applicable to a linearization of a non-linear system around a certain steady-state condition, provided that the imposed perturbations of nominal inputs are either small or slow compared with the local dynamics [5]. Therefore a linearization has been performed on the set of equations presented in Section 3, leading to the following matrix system formulation:

$$\begin{cases} \dot{x} = Ax + Bu \\ y = Cx + Du \end{cases} \quad (14)$$

where *x* is the vector of the state variables, *u* is the input vector, *y* is the output vector. This allows to focus on the state matrix *A* and its eigenvalues, which represent the carriers of the dynamic response of the system; the latter, alternatively defined as poles or roots of the system, have been calculated through dedicated MATLAB® scripts. The position of the poles and their trajectories across the Gauss plane describe the dynamic behaviour of the reactor and its variations: in order for the system to be stable, all the roots of the characteristic equation must have negative real parts, or, in term of Transfer Function (TF), all the poles must remain in the left hand side of the Gauss plane in any working condition and following any perturbation of the nominal parameters, as discussed in the ensuing case studies.

4.2 Results

A thirteenth order system has been obtained by implementing Eqs. (1) to (7) and (12). The LTI model has been Laplace-transformed and TFs have been drawn. The system has turned out to be stable at full power, as all its poles have strictly negative real part, the dominant one being located at -0.039951 rad s^{-1} (Table 2). As depicted in Figure 2, all the roots lay on the left hand side of the Gauss plane, confirming that the core is stable on the entire power range. More in detail, the neutronics-related pole is located in the origin when the reactor is at zero power conditions (green marker), and moves to the left as the power rises (red marker), granting a higher margin of stability to the system at full power. At a certain power level two poles become complex conjugated, indicating that power fluctuations occur: more in detail, the dominant

thermo-dynamics pole and the third neutronics pole - and thus the respective dynamics - reach the same velocity, becoming part of a resonance. The imaginary part of the poles increases along with the rising power level, meaning that the frequency of the oscillations increases too. This phenomenon ensues from the fact that in the linearized model the gain of the thermal feedback is proportional to the power level; thus, for equal variations of reactivity, the oscillation frequency grows as the power increases. However, despite the rise of the imaginary part of the poles, the magnitude of the real negative part grants the damping of such oscillations, which consequently result not harmful for the stability of the whole system.

Pole	Value	Units
P_1	-0.039951	rad s^{-1}
P_2	-0.015812	rad s^{-1}
P_3	-0.093171 - 0.052156i	rad s^{-1}
P_4	-0.093171 + 0.052156i	rad s^{-1}
P_5	-0.185100	rad s^{-1}
P_6	-0.614540	rad s^{-1}
P_7	-0.970330	rad s^{-1}
P_8	-1.601000	rad s^{-1}
P_9	-5.596600	rad s^{-1}
P_{10}	-12.99300	rad s^{-1}
P_{11}	-42.40900	rad s^{-1}
P_{12}	-242670.0	rad s^{-1}
P_{13}	-62125.00	rad s^{-1}

Tab 2. ELECTRA dynamic system eigenvalues (or poles)

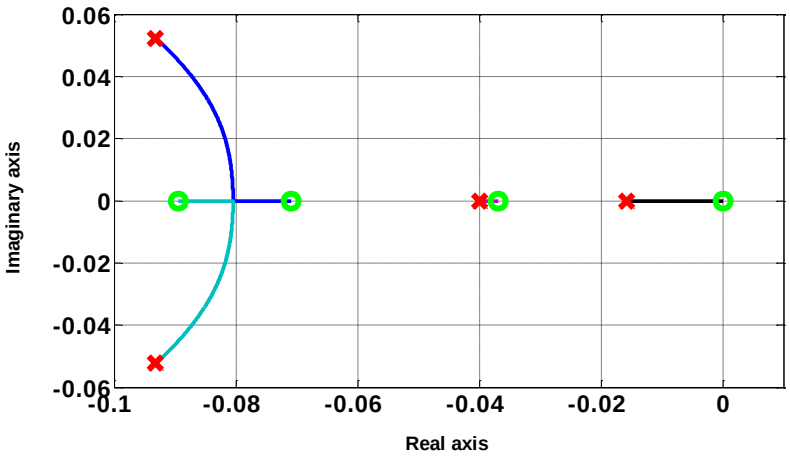

Fig 2. Root locus for ELECTRA core system as a function of power level

The core system stability has been investigated also when making the Doppler constant vary in discrete steps from its slightly negative nominal value up to + 100 pcm, so as to verify if the system is robust to uncertainties affecting this safety parameter.
As shown in Figure 3, the blue, black and purple tracks represent the poles trajectory as a function of power level (from 0 to 0.5 MW_{th}) with the Doppler constant kept at its nominal value. The red lines represent the poles trajectories evaluated at discrete power levels as a function of k_D. In this latter case, for increasing values of the respective coefficient, the roots move to the right, not becoming positive, though: it has been seen that – with all the other parameters kept at their nominal values - the system becomes unstable only for k_D higher than 1000 pcm, a clearly

non-realistic condition. Therefore, it can be stated that the system is inherently stable, and consequently safe, both at low power levels and in the case of positive Doppler coefficients.

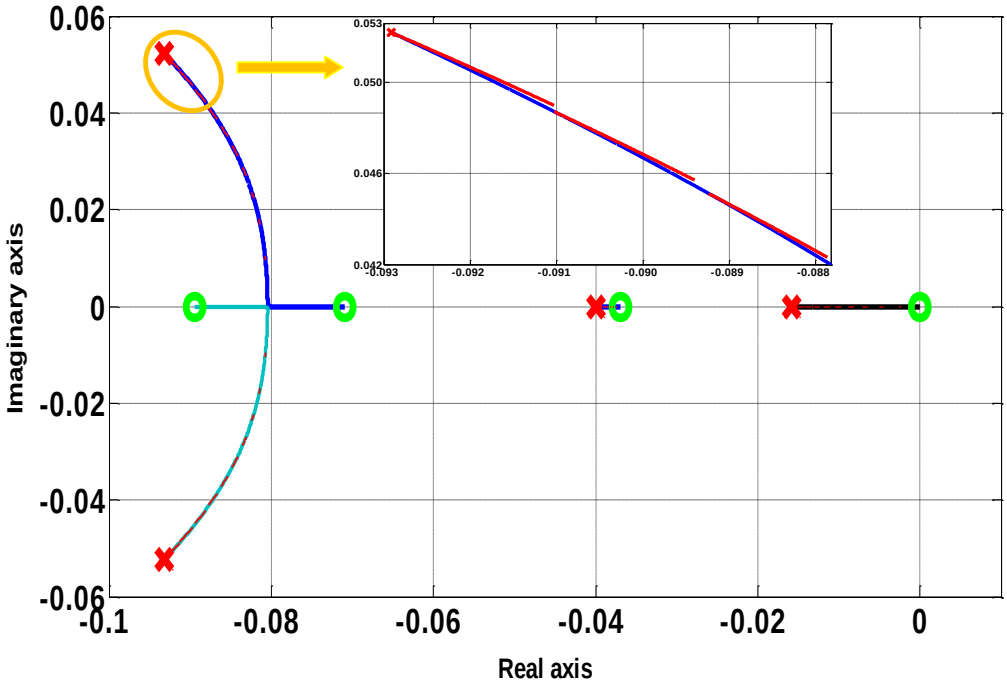

Fig 3. Root locus for ELECTRA core system as a function of power level with – 6 < k_D < 100 pcm

5. Core dynamics

Three scenarios have been simulated to analyze the core dynamic behaviour of ELECTRA. As a first transient, a control drum slight rotation has been reproduced by a positive reactivity insertion. A second transient has been initiated by acting on the total pressure loss coefficient so as to simulate an accidental enhancement of pressure drop. As a last case, a change of conditions occurring on the SG side and causing an enhancement of the coolant core inlet temperature has been assumed.

The linearized state-space model has been employed to perform transient analyses which have been compared with the reference non-linear results to provide a measure of the suitability of such a procedure in the case of a strongly non-linear system. Discrepancies between the two models have turned out to be definitely negligible under the hypothesis of small and/or slow perturbations, as shown in the next paragraphs, confirming the applicability of the linear method for investigating ELECTRA open-loop stability.

5.1 Reactivity insertion

A 26.7 pcm (0.1 $) positive reactivity stepwise insertion has been simulated at time t = 200 s. As highlighted in Figure 4, the expected power response is observed, *i.e.* the initial, instantaneous power rise (prompt jump). Such a behaviour is found in the transient evolution of all the variables of interest, which exhibit monotonous increases with analogous time characteristics, which are mainly influenced by reactivity feedback coefficients.

After the power sudden rise at the very beginning of the transient, fuel, cladding and coolant temperatures start increasing monotonically, balancing the reactivity introduced by control drums. In the case of a positive Doppler constant, the fuel temperature enhancement contributes positively to the total reactivity; however, such an effect is largely compensated by the remaining

sizable feedbacks, resulting in an impact of less than 2 % on the total power rise, and of approximately 2 °C on temperatures (in the most conservative scenario of k_D = 100 pcm).
Owing to the outlet lead temperature rise, an increase of lead mass flow rate occurs brought by the thermal head enhancement. The latter results in an additional feedback to the system, since the primary effect of a coolant mass flow rate increase would be a reduction of all temperatures in the system. In the present case, the superposition of the feedbacks ensuing from both the mentioned effects leads to an increase of power combined with a minor temperatures enhancement if compared with a forced circulation case, though. In fact, the presence of natural circulation causes a further rise of power when a reactivity insertion occurs, but resulting in better conditions for cladding and coolant temperatures.

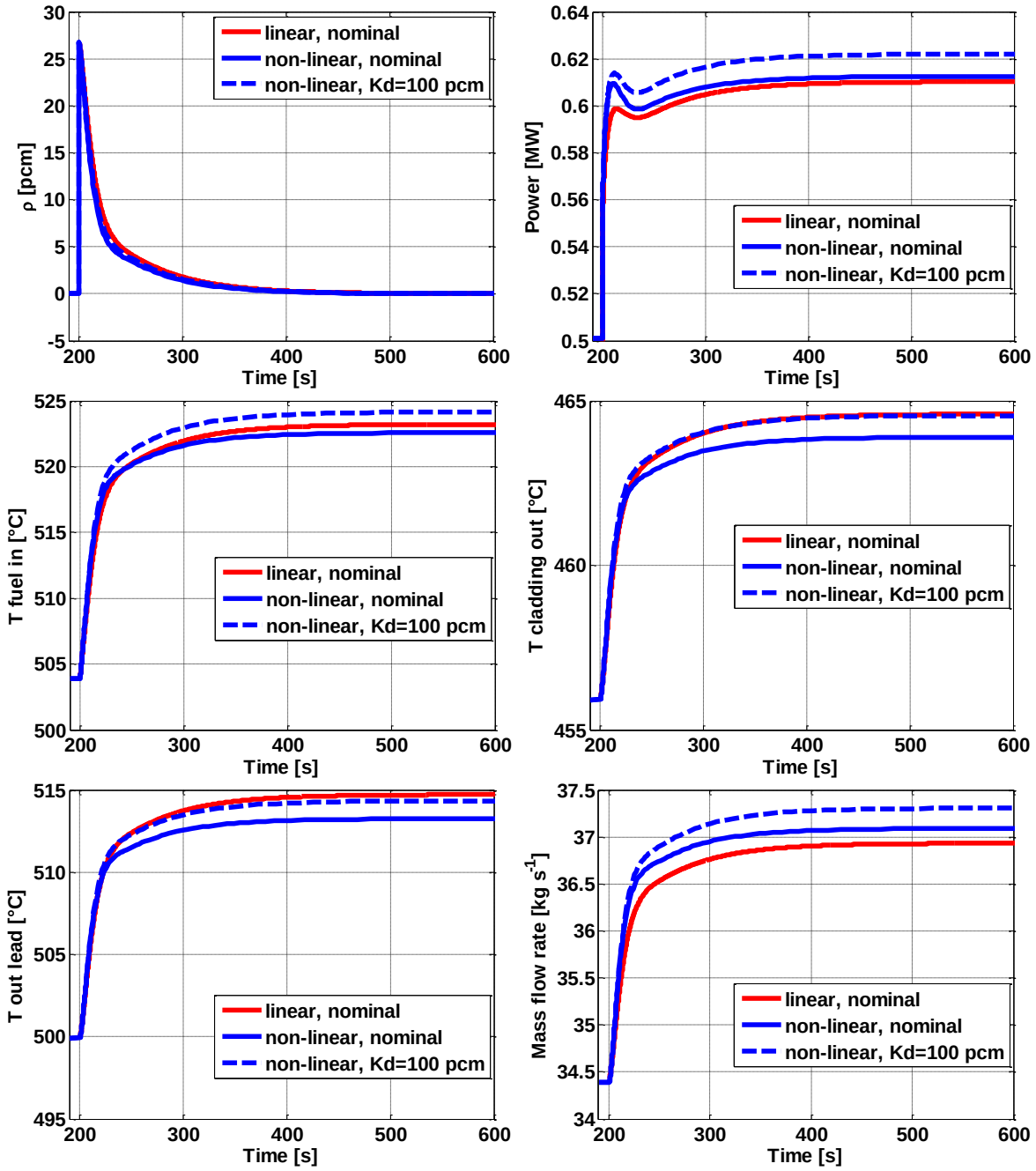

Fig 4. ELECTRA main variables time-response following a 0.1 $ stepwise reactivity insertion

5.2 Pressure drop enhancement

A 10 % stepwise enhancement of the total pressure loss coefficient (corresponding to 1.451) has been imposed at time t = 200 s to simulate the occurrence of a partial channel blockage (Figure 5). As an immediate effect, the coolant mass flow rate decreases leading to a sudden increase of lead, cladding and fuel temperatures, which, in turn, brings an insertion of negative reactivity due to all the feedback effects.

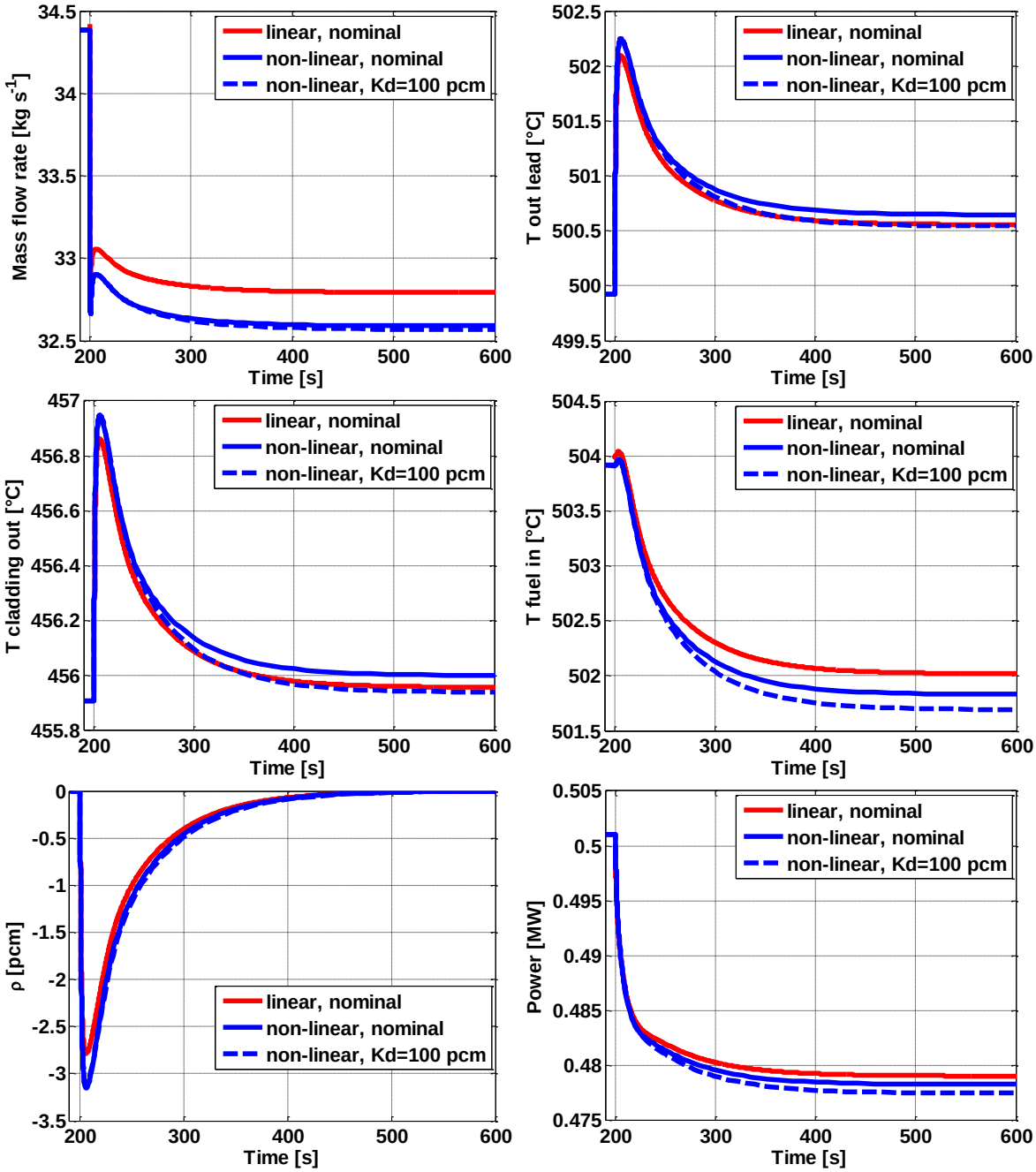

Fig 5. ELECTRA main variables time-response following a 10 % stepwise enhancement of the total pressure loss coefficient

Therefore, the core power starts decreasing and consequently the fuel temperature undergoes a reduction, settling at a lower steady-state value than nominal, whereas cladding and coolant

stabilize at slightly higher values owing to the reduced mass flow rate. Such a transient evolution is very similar to a classical Unprotected Loss of Flow scenario for a forced circulation system. Also in this case study the impact of uncertainties affecting the Doppler constant is definitely negligible, the core transient behaviour resulting only very slightly influenced by a positive Doppler effect even in the most conservative scenario.

5.3 Core inlet temperature variation

The last simulation involves the core inlet temperature, which has been enhanced by 10 °C at time t = 200 s (Figure 6).

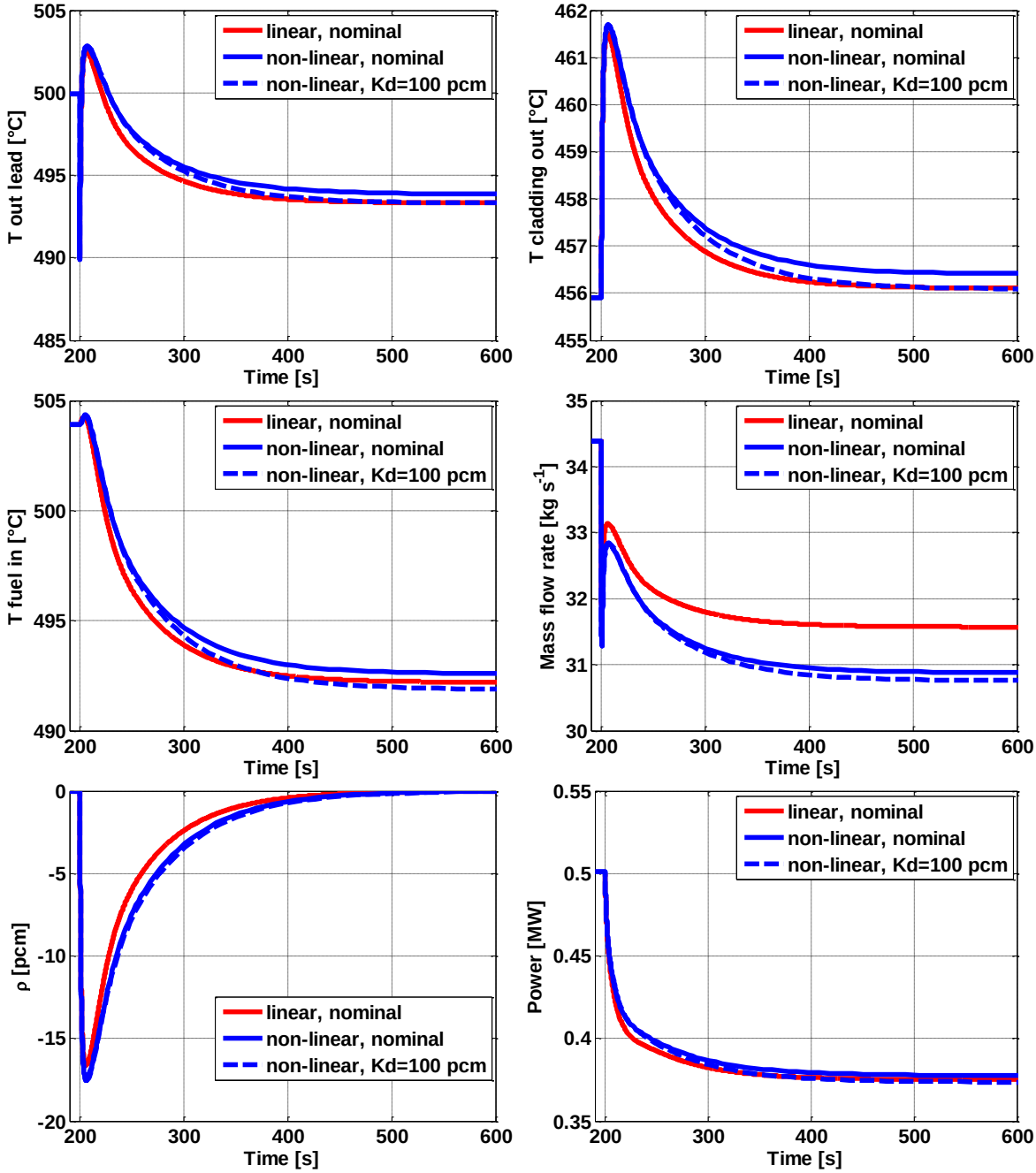

Fig 6. ELECTRA main variables time-response following a 10 % stepwise coolant inlet temperature increase

As a result of this stepwise perturbation, the system characteristic temperatures immediately rise up. Such an effect is magnified by natural circulation because of the head decrease provided by buoyancy, which causes an instantaneous mass flow rate reduction with consequent additional increasing effect on temperatures. Owing to the negative reactivity injection brought by reactivity feedbacks, the power undergoes a decrease. Due to the lower power produced within the core, the fuel temperature decreases in turn, settling at a lower steady-state value, whereas the cladding temperature results slightly increased.
For this crucial simulation - which is actually the most likely to occur, since it reproduces either a malfunction or, more in general, a change of the heat exchange conditions on the plant secondary side - natural circulation acts unfavourably. In this kind of scenario, in fact, it is important to keep temperatures low while avoiding troublesome oscillations, in particular as far as the cladding temperature is concerned. In presence of natural circulation, the decrease of mass flow rate induces a further enhancement of peak temperatures leading to an additional stress for materials. Nevertheless, in ELECTRA this effect is mitigated by the choice of a nitride fuel featuring favourable thermal properties.

6. Conclusions

In this paper a preliminary stability and dynamics analysis of the current core configuration of ELECTRA has been presented. A simulation tool has been developed expressly meant for such an early phase of the reactor conceptual design, aimed at evaluating the robustness and stability of the dynamic system itself on its entire power range, and at performing design-basis transient analyses.
Despite the strong non-linearities characterizing the constitutive equations, discrepancies between the reference model and its linearized version have turned out to be definitely negligible under the hypothesis of small or slow perturbations, confirming the linear method applicability to investigate ELECTRA open-loop stability.
As a major outcome of this study, the system has turned out to be inherently stable on the entire power range independently of uncertainties affecting the value of the Doppler constant, which should reach unrealistic high values (nearly 1000 pcm) to make the core unstable. Of course these preliminary results are to be verified by implementing a full model of ELECTRA incorporating also the remaining components (such as bypass channels, cold and hot legs, and in particular SGs), so as to investigate the effects - either stabilizing or destabilizing - induced by both the coupling with the secondary system and time delays.
Furthermore, the core response to some typical transient initiators has been investigated by introducing 10 % positive variations of reactivity, total pressure loss coefficient and coolant core inlet temperature. As anticipated by the stability analyses outcomes, absolutely minor discrepancies have been found in the core dynamic behaviour when employing the nominal Doppler constant or when assuming a large positive value. In addition, all the technological constraints (namely, peak fuel and cladding temperatures) have resulted to be respected with sufficiently wide safety margins, confirming the system has been properly designed to guarantee enhanced passive safety features ensuing from both suitable reactivity coefficients and an effective core cooling capability.

7. References

[1] J. Wallenius, E. Suvdantsetseg, A. Fokau, 2012. ELECTRA: European Lead Cooled Training Reactor. Nuclear Technology, 177, 3.
[2] E. Suvdantsetseg, J. Wallenius, S. Bortot, 2012. Optimization of the reactivity control drum system of ELECTRA. Nuclear Engineering and Design, 252.
[3] The MathWorks, Inc. (2007).

[4] E. Bubelis, M. Schikorr, 2008. Review and Proposal for Best-fit of Wire-wrapped Fuel Bundle Friction Factor and Pressure Drop Predictions Using Various Existing Correlations. Technical Report FZKA 7446.
[5] A. M. Lyapunov, 1968. Stability of motion. New York and London Academic Press.

8. Nomenclature

A Coolant area in the active core [m^2]
C Average specific isobaric heat [J kg^{-1} K^{-1}]
c_i i^{th} precursor density [cm^{-3}]
d Density [kg m^{-3}]
g Gravitational acceleration [m s^{-2}]
h_{cl} Clad-coolant global heat transfer coefficient [W K^{-1}]
k_c Cladding thermal conductivity [W m^{-1} K^{-1}]
K_c Core total pressure loss coefficient [-]
k_D Doppler constant [pcm]
k_f Fuel thermal conductivity [W m^{-1} K^{-1}]
k_g Helium gap thermal conductivity [W m^{-1} K^{-1}]
L Core active height [m]
M Mass [kg]
n Neutron density [cm^{-3}]
P Pressure [Pa]
q Reactor thermal power [MW]
t Time [s]
T Average temperature [°C]
Z Coolant quote [m]
α_L Coolant density reactivity coefficient [pcm K^{-1}]
α_R Radial expansion reactivity coefficient [pcm K^{-1}]
α_Z Axial expansion reactivity coefficient [pcm K^{-1}]
β Total delayed neutron fraction [pcm]
β_i i^{th} precursor group delayed-neutron fraction [pcm]
Γ Coolant mass flow rate [kg s^{-1}]
δ Isobaric thermal expansion coefficient [K^{-1}]
Λ Invariant neutron lifetime [s]
λ_i i^{th} precursor decay constant [s^{-1}]
ρ Reactivity [pcm]

Superscripts and subscripts

0 Steady-state
acc Accelerative
c Cladding
centr Centerline
drum Control drum
eff Effective
f Fuel
in Inlet
int Internal
l Lead coolant
loss Losses
mid Middle
out Outlet
surf Surface

ANALYSIS OF THE TUBES-TO-TUBESHEET CREVICES UNDER THE OPERATING CONDITIONS OF THE AP1000 PRHR-HX

ANDREA BARBENSI
Design of Special Components, Ansaldo Nucleare S.p.A,
Corso F.M. Perrone, 25, IT-16152, Genoa, Italy

ABSTRACT

Like the conventional PWR Steam Generators, the Tubesheet (T/S) of the AP1000 Nuclear Power Plant Passive Residual Heat Removal Heat Exchanger (PRHR-HX) is made of low alloy steel and the tubes of Inconel 690. The tubes are seal welded to the T/S primary side Inconel cladding and then they are hydraulically expanded over the entire thickness of the T/S. This process is intended to reduce to the minimum the crevice between tubes and T/S holes, which historically has been source of several corrosion issues.

For the PRHR-HX the risk associated with the presence of crevices is even higher, since this HX has no secondary side shell and is directly immersed in the In-Containment Refueling Water Storage Tank (IRWST), which contains aerated, borated water, used both for refueling operations and as a heat sink for the HX. For this reason also the secondary side of the T/S is cladded with a layer of Stainless Steel, to prevent borated water from reaching the base metal.

This paper describes:
a) the methodology and calculations performed to simulate the complex tube behaviour during the hydraulic expansion process and during the various operating conditions (tube deformation and residual stresses, T/S bowing effect, differential thermal expansion)
b) the definition of a possible Test Facility aimed to confirm experimentally the analytical results.

Results of the performed analysis allow to say that there is no risk of opening of the crevices (not greater than 3.175 mm [0.125 in]) that may jeopardize the Tube-to-Tubesheet joint.

Keywords: PRHR-HX, Tube-to-Tubesheet Joint, Hydraulic Expansion, Crevice.

1. Introduction

The PRHR HX [1] is an integral part of the innovative PXS of the Generation III+ AP1000 Nuclear Power Plant (WEC Owner design), whose function is to remove the reactor core decay heat, maintaining the NPP in a safe shutdown condition. The HX - measuring approximately 9 meters [29.5 ft] in height, 6 meters [19.7 ft] in depth, 2.5 meters [8.2 ft] in width, and weighting 43 tons [94.8 Kips] - is completely submerged in a 2200 m^3 [77692 ft^3] water storage tank located inside the containment vessel (IRWST), and is elevated above the reactor coolant loop to induce natural circulation flow when called into operation.
The HX consists of an inlet and outlet channel head in low alloy steel forgings with stainless steel cladding. The Tubesheets are cladded with Inconel and stainless steel cladding of the surfaces in contact respectively with the RCS and the IRWST. Each T/S houses 689 “C-shaped” tubes joined to the T/S itself using the same technology of the Steam Generators, i.e. seal weld on the primary side and full depth hydraulic expansion which minimizes tensile residual stresses in the transition zone and reduces the depth of the crevice on the secondary side.

author’s email: andrea.barbensi@ann.ansaldo.it

The HX has no secondary shell and is exposed to the IRWST borated water (see Fig. 1). Since the pressure inside the channel head induces a bending deformation of the T/S, which may enlarge the (small) crevices, the potential risk exists that corrosive fluid come into contact with the T/S material.
However, during plant normal operating condition, the primary side pressure induces a T/S bowing, causing a deformation of the holes (i.e. a diameter increase) that is maximum for the center hole and that increases the depth of the tube-to-T/S crevice. On the other hand, this effect is in turn opposed by the enlargement of the tube outside diameter, caused by a) the internal pressure; b) the release of the hydraulic expansion compressive stresses in the tube and c) by the two materials differential thermal expansion.

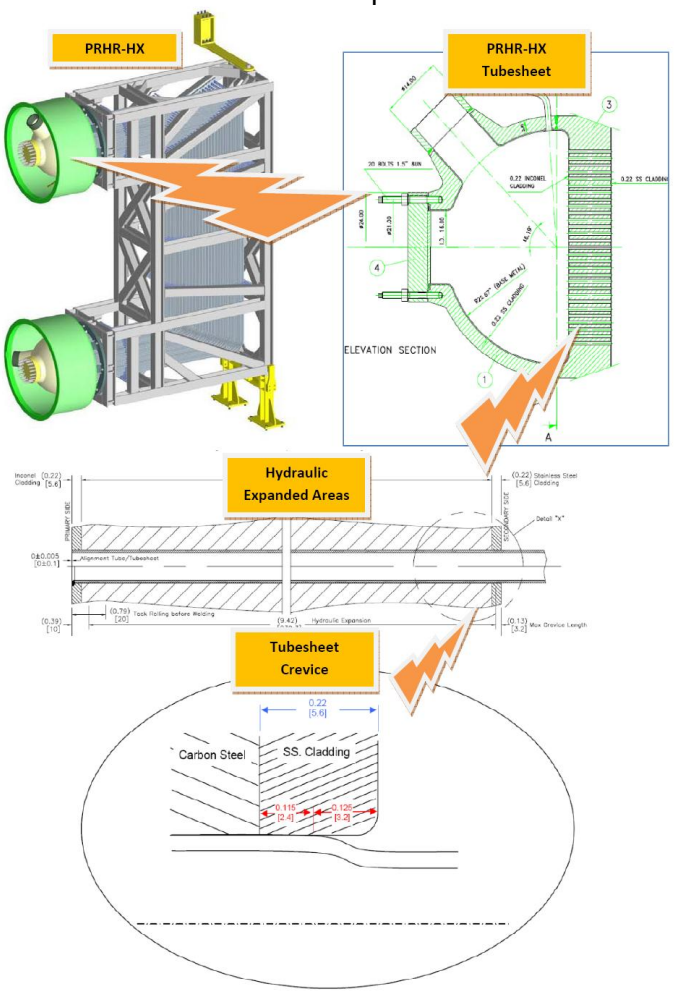

Fig 1. PRHR HX Tube-to-Tubesheet Joint

The paper describes two methodologies – one analytical and one experimental – to show that being the T/S secondary side covered with a 5.6 mm [0.22 in] thick SS cladding, a design crevice not greater than 3.175 mm [0.125 in] avoids under the HX operating conditions the contact of the low alloy steel T/S material with the IRWST borated water.

2. Tube-to-Tubesheet Joint FEM Analysis

The hydraulic expansion of the Tube-to-Tubesheet joint is a complex and highly non-linear problem. This non-linearity arises from three distinct sources: material non-linearity because of the tube elastoplastic behavior, geometric non-linearity due to the large strains and displacements, and finally the boundary condition non-linearity as a result of the contact interaction between the tube outer surface and the T/S hole. Each of these non-linearities has to be dealt with carefully in order to obtain useable and reliable results. The model developed is a 2D axisymmetric one, which includes the Channel Head, the T/S and the central tube (see Fig. 2). ANSYS [2] computer program version 9.0 has been used. The tube material is elastic-plastic with kinematic work hardening coefficient. Different values of

expansion pressure were analyzed, to investigate the effect on the residual stresses, tube-hole interference and possible yielding of the T/S ligaments around the pressurized tube.
The material properties and geometric parameters are described in Table 1.

TUBE	Outside Diameter	0.75+0/-.008 in. (19.05 mm)
	Wall Thickness	0.065 in. (1.65 mm)
	Material	SB 163 N06690
	Sy	40 ksi (276 MPa)
TUBESHEET	Hole Diameter	0.758±0.002 in. (19.25 mm)
	Nominal Depth	9.5 in. (241.3 mm)
	Material	SA 508 Gr. 3 Cl. 2
	Sy	65 ksi (448.3 MPa)
FABRICATION	Hydraulic Expansion Pressure	36.2-43.51 ksi (250-300 MPa)
	Crevice Depth	1/32 – 1/8 in. (0.8 – 3.2 mm)

Tab 1. Tube-to-Tubesheet Joint Geometric, Material, Fabrication Parameters

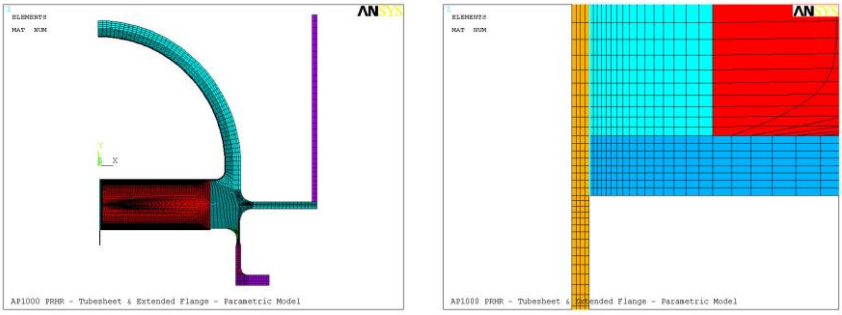

Fig 2. FEM Analysis Models

Results in terms of tube profile and residual stresses in the transition zone are shown in Fig. 3 for an hydraulic pressure of 300 MPa [43.51 ksi]. For both hoop and axial directions the pattern of stress distribution was shown to be similar and closely predicted by the analysis [3]. The location of the hoop stress peak is the end result of a complex interaction and equilibration of elastic and plastic deformations within a small axial length of the thin walled tube. The hoop stress peak tends to be limited to a narrow circumferential band (< 2.5 mm [0.1 in]) at the middle of the slope between the so called "heel" and "toe" of the transition zone. The location of the axial stress peak is found closer to the heel location where bending stresses would be expected.
A further step of the analysis shows that during the primary side pressurization (channel head and tubes) corresponding to PRHR HX standby conditions (15.5 MPa [2250 psia]), no loss of contact occurs on Tube-to-Tubesheet Joint.

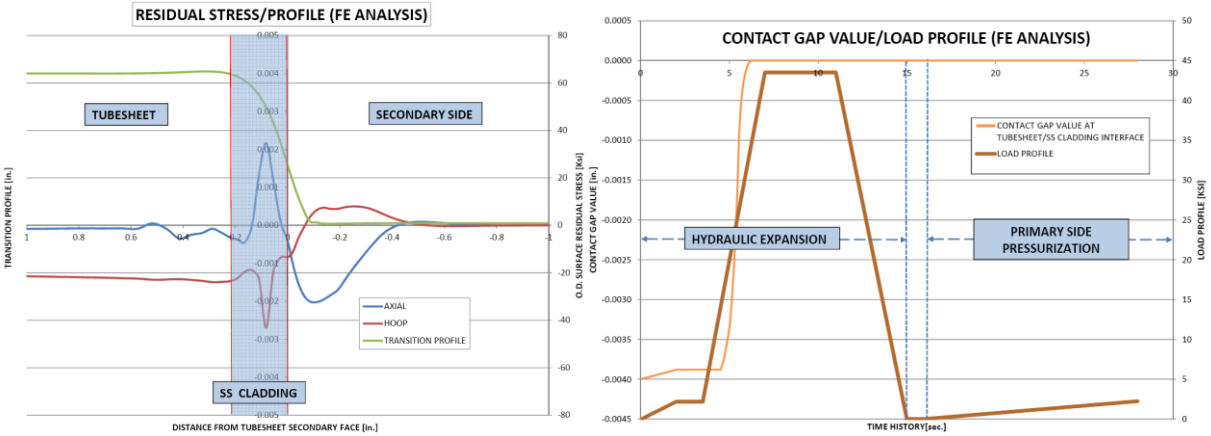

Fig 3. FEM Analysis Results

The FE modelling provides two observations significant to further joint tightness assessment:
1. Tube to hole contact pressure can be accurately predicted by analytical modeling.

2. Variation in expansion pressure to achieve increased joint contact pressure can proceed with minimal penalty to residual stress. It has been shown that variation of expansion pressure (to achieve objectives for leak tightness, and pullout strength) results in only small penalty in residual stress at the expansion transition.

3. Tube-to-Tubesheet Joint Mockup Design

Considering that the internal pressure causes in the T/S a biaxial state of bending stresses through the thickness (tension on the secondary side, where the crevices are present), the phenomenon can be properly investigated by using a mockup limited to a layer of the T/S only, subject to a membrane state of tensile stresses equal to the maximum of the actual configuration.

The proposed test mockup (Fig. 4) is a square plate, 30 mm [1.18 in] thick, with a central test hole containing an expanded tube, surrounded by eight additional holes and prototypical ligaments. This mockup will be loaded by a set of forces applied to the dummy holes in order to reproduce around the test hole the maximum state of stress of the central part of the T/S under primary operating pressure

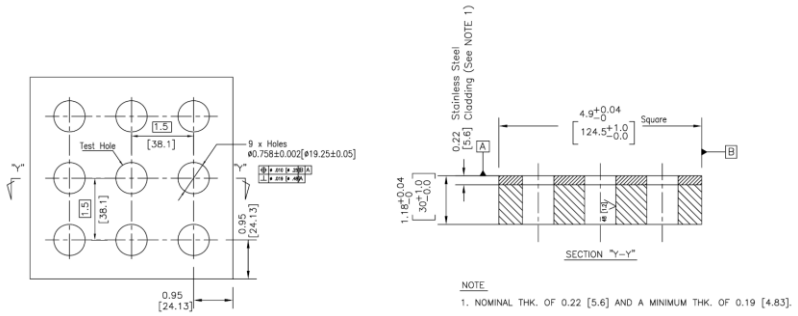

Fig 4. Proposed TEST Coupon

The Fig. 5 shows the methodology followed to define this set of forces.

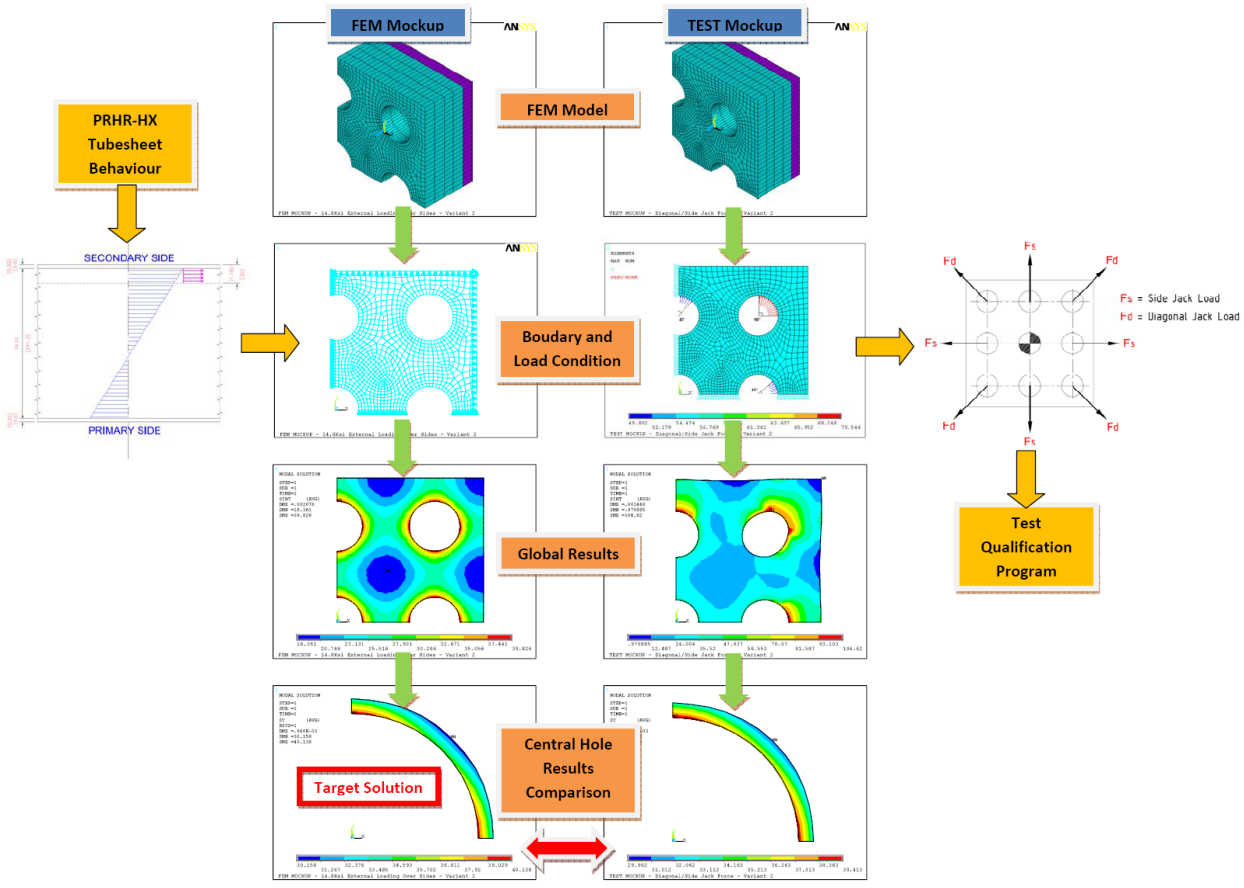

Fig 5. Tube-to-Tubesheet Joint Mockup Design Method

The complete axial symmetric Finite Element model of the Channel Head and T/S was first used to evaluate the maximum deformations and stresses in the T/S ligaments, following the ASME III Appendix A-8000 methodology (equivalent solid plate and ligament efficiency). Then, a detailed 3D model of the mockup, including the nine holes and the cladding, was defined (called FEM Mockup model). Taking advantage of the symmetry, only a quarter of the structure was modeled with proper boundary conditions. This model was subjected to an imposed outward displacement at the edges with an iterative process until the calculated stress distribution and displacement around the test hole match the corresponding values of the global model analysis with reasonable approximation.
Finally, a Test Mockup model (basically the same as the FEM Mockup model) was analyzed: forces (to be obtained by jacks) are applied to the eight dummy holes and changed in value until the same stress distribution and displacement around the test hole of the FEM Mockup model are obtained.

4. Tube-to-Tubesheet Joint Test Facility Design

The proposed test facility to perform the Tube-to-Tubesheet joint qualification program is shown in Fig 6. The test mockup will be obtained by cutting a 30 mm [1.18 in] thick “slice” from a full thickness T/S sample, cladded and drilled according to the final production procedures. The central hole will house a piece of tube hydraulically expanded with the production process. Before starting the test, a profilometry will be conducted of the internal surface of the expanded tube in order to measure the actual geometry of the crevice.

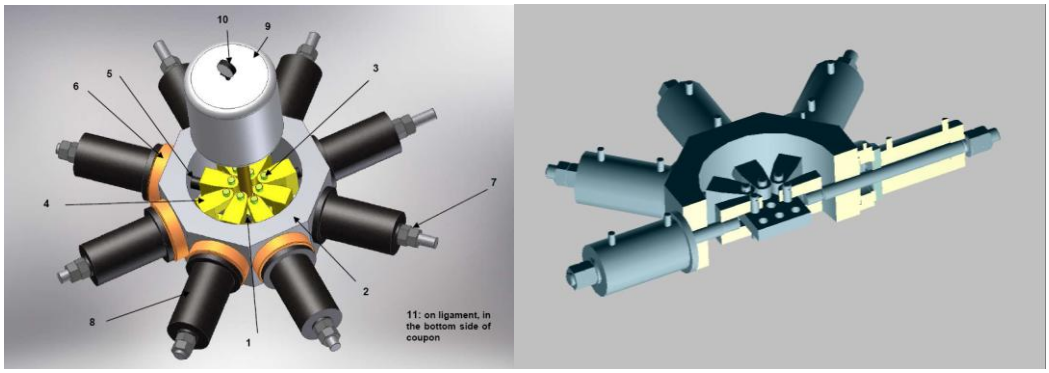

Fig 6 Tool for tension test

1 - Tension test coupon; 2 - Carbon steel support structure; 3 - Pin; 4 - U strap;
5 - Tie rods; 6 - Load cell; 7 - Nuts and washer; 8 - Hydraulic jacket; 9 - Stainless steel chamber for borated water; 10 - Pressure gauge; 11 - Strain Gauge

The eight dummy holes will be used to connect with pins eight hydraulic jacks, whose force is reacted by an ad-hoc-designed-octagonal-shape structure. Load cells between the jacks and this structure will be used to measure the applied loads. Strain gages in the ligaments around the tube will monitor the stresses. The tube can be pressurized to the operating pressure, or, conservatively, can be at atmospheric pressure. A stainless steel chamber on the cladded surface of each test sample will simulate the IRWST conditions: aerated borated water (2700 ppm boron) at IRWST maximum hydrostatic pressure. A dye can be added to help in the post test metallographic assessment. Furthermore, the pressure can be increased (three times the actual one seems a reasonable value) to make the test even more severe. Pressure holding time (10 hours minimum) is established to compensate for the extremely small quantities of fluid that might potentially leak into the Tube-to-Tubesheet annulus. Pressure is the chamber and presence of liquid on the lower side of the mockup is checked by visual in order to avoid macroscopic leakage. Several mockups will be tested, to cover the various tolerances (tube diameter, hole diameter, surface roughness, expansion pressure, etc.). After completion of testing, all test samples will be sectioned and subjected to metallographic examination to determine if there has been an ingress of boric acid fluid into the joint and, if yes, the depth of penetration.

The test will be considered successful if:

- No leakage of borated water is detected in the Tube-to-Tubesheet annulus area, checked, with visual examination, and through a pressure value measurement inside the borated water chamber, at the end of the holding time.
- No trace of colored dye present beyond the Tube-to-Tubesheet crevice where fluid was exposed to the carbon steel internal surface shall be present on the sectioned samples.

5. Conclusion

During PRHR HX operation, the pressure-induced strains of the T/S secondary side holes reduce the positive contact pressure obtained by the hydraulic expansion process. Reduction below a critical minimum value will allow penetration of IRWST borated water into the crevice, with risk of corrosion of the T/S material. On the other side, the tube to hole contact pressure is enhanced by the tube internal pressure and differential thermal expansion between the tube and the T/S material.
The finite element method can be used to properly model the tube to hole contact pressure around the tube circumference both as consequence of the hydraulic expansion and during the operating conditions. Results of the performed analysis allow to say that there is no risk of opening of the crevices that may jeopardize the Tube-to-Tubesheet joint. The analytical approach has been used also to define a test mockup to be a can simulate with very good approximation the actual phenomena. Finally, a possible configuration of the overall test facility and a preliminary qualification program has been defined.

6. Acknowledgements

The author wishes to thank for his precious contribution Mr. Flavio Magris, Manager of Special Components Design & Analysis Department at ANN.

7. Nomenclature

ANN	Ansaldo Nucleare S.p.A.
FEM	Finite Element Modelling
IRWST	In Containment Refueling Water Storage Tank
NPP	Nuclear Power Plant
PRHR-HX	Passive Residual Heat Removal Heat Exchanger
PXS	Passive Core Cooling System
RCS	Reactor Coolant System
SCC	Stress Corrosion Cracking
SG	Nuclear Steam Generator
T/S	Tubesheet
WEC	Westinghouse Electric Corporation

8. References

[1]. EPS-GW-GL-700, Revision 1, AP1000 Design Control Document (DCD). https://www.ukap1000application.com/doc_pdf_library.aspx
[2]. ANSYS® Mechanical, Release 9.0, Documentation for ANSYS, ANSYS Inc.
[3]. McGregor, R., Abdelsalam, U., “Experimental Residual Stress Evaluation Of Hydraulic Expansion Transitions In Alloy 690 Steam Generator Tubing”, Seventh International Symposium on the Degradation of Materials in Nuclear Power Systems – Water Reactors, (Breckenridge, Colorado, August 7-10, 1995). http://www.lambdatechs.com/documents/216.pdf

European Nuclear Society
Rue Belliard 65
1040 Brussels, Belgium
Telephone: +32 2 505 30 50 - FAX: +32 2 502 39 02
enc2012@euronuclear.org
www.enc-2012.org

□